JGR Solid Earth

RESEARCH ARTICLE
10.1029/2020JB020982

Limited Mantle Hydration by Bending Faults at the Middle America Trench

Nathaniel C. Miller[1], Daniel Lizarralde[2], John A. Collins[2], W. Steven Holbrook[3], and Harm J. A. Van Avendonk[4]

[1]U.S. Geological Survey, Woods Hole Costal and Marine Science Center, Woods Hole, MA, USA, [2]Department of Geology and Geophysics, Woods Hole Oceanographic Institution, Woods Hole, MA, USA, [3]Department of Geosciences, Virginia Polytechnic Institute and State University, Blacksburg, VA, USA, [4]Jackson School of Geosciences, University of Texas Institute for Geophysics, Austin, TX, USA

Key Points:

- Upper mantle anisotropy indicates that hydration by fluid flow along bending faults is limited to fault zones that thin with depth
- Confining hydration to fault zones reduces estimates of water storage by an order of magnitude
- A dry, intermediate-age slab mantle suggests that hydration may be globally limited by fault dynamics, rather than temperature

Correspondence to:
N. C. Miller,
ncmiller@usgs.gov

Citation:
Miller, N. C., Lizarralde, D., Collins, J. A., Holbrook, W. S., & Van Avendonk, H. J. A. (2021). Limited mantle hydration by bending faults at the Middle America Trench. *Journal of Geophysical Research: Solid Earth*, *126*, e2020JB020982. https://doi.org/10.1029/2020JB020982

Received 11 SEP 2020
Accepted 1 DEC 2020

Abstract Seismic anisotropy measurements show that upper mantle hydration at the Middle America Trench (MAT) is limited to serpentinization and/or water in fault zones, rather than distributed uniformly. Subduction of hydrated oceanic lithosphere recycles water back into the deep mantle, drives arc volcanism, and affects seismicity at subduction zones. Constraining the extent of upper mantle hydration is an important part of understanding many fundamental processes on Earth. Substantially reduced seismic velocities in tomography suggest that outer rise plate-bending faults provide a pathway for seawater to rehydrate the slab mantle just prior to subduction. Estimates of outer-rise hydration based on tomograms vary significantly, with some large enough to imply that, globally, subduction has consumed more than two oceans worth of water during the Phanerozoic. We found that, while the mean upper mantle wavespeed is reduced at the MAT outer rise, the amplitude and orientation of inherited anisotropy are preserved at depths >1 km below the Moho. At shallower depths, relict anisotropy is replaced by slowing in the fault-normal direction. These observations are incompatible with pervasive hydration but consistent with models of wave propagation through serpentinized fault zones that thin to <100-m in width at depths >1 km below Moho. Confining hydration to fault zones reduces water storage estimates for the MAT upper mantle from ~3.5 wt% to <0.9 wt% H_20. Since the intermediate thermal structure in the ~24 Myr-old MAT slab favors serpentinization, limited hydration suggests that fault mechanics are the limiting factor, not temperatures. Subducting mantle may be similarly dry globally.

1. Introduction

Bending of the lithosphere during subduction extends the oceanic crust and uppermost mantle, producing outer rise normal faults (Masson, 1991). Seismic images indicate that these faults may reach down to ~8–10 km into the mantle (Han et al., 2016; Ranero et al., 2003), suggesting that the plate is in extension to similar depths. This extension may create subhydrostatic dynamic pressures along bending faults, driving downward flow that, according to numerical models, pumps seawater up to ~10 km into the mantle (Faccenda et al., 2009). If seawater does reach the mantle, it would occupy pore space and react strongly with olivine, producing the hydrous mineral serpentine (Faccenda, 2014; Peacock, 1990). A serpentinized upper mantle can deliver water to deeper depths than water stored in sediments and the crust (Rupke, 2004; van Keken et al., 2011). Upper mantle serpentinization during outer rise faulting thus has the potential to be a principal source of water delivered to the deep mantle and a large component of the global-scale water cycle.

Observational constraints on the extent of outer rise hydration (i.e., serpentinization) have come largely from controlled-source, isotropic seismic tomography that shows ~5–10% reductions in compressional velocities (V_p) in the upper ~1–10 km of the mantle at a variety of subduction zones (Grevemeyer et al., 2018). These slow seismic velocities have been interpreted as evidence that seawater flow along bending faults routinely and significantly rehydrates the upper mantle just prior to subduction (Grevemeyer et al., 2018). At the Middle America Trench (MAT) offshore Nicaragua, a site central to development of the outer rise hydration hypothesis (Ranero et al., 2003), comparing V_p of ~7.0–7.2 km/s from tomography to laboratory measurements of ~7.9–8.2 km/s mean (isotropic) wavespeeds for unaltered peridotites yields an estimate of ~30% serpentinization by volume (Van Avendonk et al., 2011), or ~3.5 wt% H_2O (Carlson & Miller, 2003)—the largest value reported from any subduction zone (Grevemeyer et al., 2018).

The high degree of hydration inferred from isotropic tomography presents challenges. If slabs are similarly hydrated globally, subduction would have consumed more than two oceans worth of seawater over the Phanerozoic, yet the geologic record indicates that eustatic sea level has only dropped by at most ~360 m over this eon (Parai & Mukhopadhyay, 2012). Controls on outer rise serpentinization do, however, vary significantly between subduction zones (Faccenda, 2014) and through geologic time (Merdith et al., 2019), and constraining global, long-term water budgets is difficult. Furthermore, secular variation in buoyancy and isostacy allows for substantial water influx to the mantle without requiring a long-term change in sea-level (Korenaga et al., 2017).

High degrees of mantle hydration also present local geodynamic problems. The buoyancy increase caused by ~10% serpentinization of the upper ~10 km of mantle (or thicker/thinner slabs with lower/higher degrees of serpentinization and equivalent mean densities) may be enough to inhibit subduction (Schmidt & Poli, 1998). Delivering water to upper mantle depths could require that the dynamic pressure reduction from faulting exceed limits based on brittle deformation theory (Korenaga, 2017). If water does reach the upper mantle, a realistic mechanism may not exist to drive horizontal flow away from fault zones with sublithostatic pressures to areas between faults, where confining pressure is higher (Korenaga, 2017), and the efficiency of upper mantle hydration by the tectonic pumping mechanism is itself also uncertain. Even if horizontal flow can be sustained, outward expansion of the reaction front requires diffusion of water through already serpentinized mantle, and the pressure dependence of serpentine permeabilities and timescales for subduction likely limit the lateral extent of outer rise upper mantle hydration to zones around faults (Hatakeyama et al., 2017).

Conversion of tomographic velocities to subduction zone water input typically assumes that slowing is caused by uniform upper mantle hydration (Grevemeyer et al., 2018), but slowing can also be produced by serpentinite (or water) filled cracks and/or wide damage zones aligned along outer rise faults (Korenaga, 2017; Miller & Lizarralde, 2016). Mean seismic wavespeeds (i.e., as measured by isotropic tomography) alone cannot distinguish between pervasive mantle hydration and alteration that is confined to fault zones. These contrasting models should, however, produce measurably different seismic anisotropy patterns. If alteration is confined to relatively narrow fault zones, we expect relict azimuthal anisotropy aligned along fast and slow directions inherited from the spreading center (Hudson et al., 2001; Miller & Lizarralde, 2016). In contrast, if alteration is pervasive, the original anisotropy would be erased and eventually replaced by serpentinization (Wallis et al., 2011). We applied this test to the outer rise at the MAT offshore Nicaragua (Figure 1) by measuring large-scale, upper-mantle anisotropy using wide-angle, controlled-source, ocean-bottom seismograph data.

2. Geophysical Constraints on Outer-Rise Hydration

Reductions in V_p have been imaged by two-dimensional, isotropic tomography in the outer rise upper mantle at the Aleutian (Holbrook et al., 1999; Shillington et al., 2015), Chile (Contreras-Reyes et al., 2007, 2008, 2014, 2015; Moscoso & Grevemeyer, 2015; Ranero & Sallarès, 2004), Japan (Fujie et al., 2018), Java (Planert et al., 2010), Kuril (Fujie et al., 2013, 2018), Mariana (Cai et al., 2018), Middle America (Grevemeyer et al., 2007; Ivandic et al., 2008, 2010; Van Avendonk et al., 2011; Walther et al., 2000), and Tonga (Contreras-Reyes et al., 2011) trenches. At all of these trenches, V_p progressively decreases when approaching the trench (Grevemeyer et al., 2018). The degree of slowing also correlates with the extent of bend faulting (Fujie et al., 2018; Shillington et al., 2015; Van Avendonk et al., 2011). At the MAT offshore Nicaragua, the outer rise is densely faulted and upper mantle velocities are ~7.0–7.2 km/s in two-dimensional, isotropic tomography (Van Avendonk et al., 2011) (Figure 1), ~10–20% slower than the ~8.2–8.4 km/s mean (isotropic) wavespeed in unaltered mantle peridotite (Christensen, 1966). Further south, along the same two-dimensional tomogram and offshore Costa Rica, outer-rise faulting is not as extreme and upper-mantle velocities are ~8.0 km/s (Van Avendonk et al., 2011), closer to the expected value for unaltered mantle.

Laboratory measurements of wavespeeds in serpentinized peridotites are slower than in unaltered peridotites (Christensen, 1966), and, at all of the trenches listed above, slow velocities have been interpreted as evidence for widespread, uniform hydration of the upper mantle. Over a wide range of temperatures and pressures, the mean (isotropic) wavespeed of a partially serpentinized peridotite can be approximated by (Carlson & Miller, 2003):

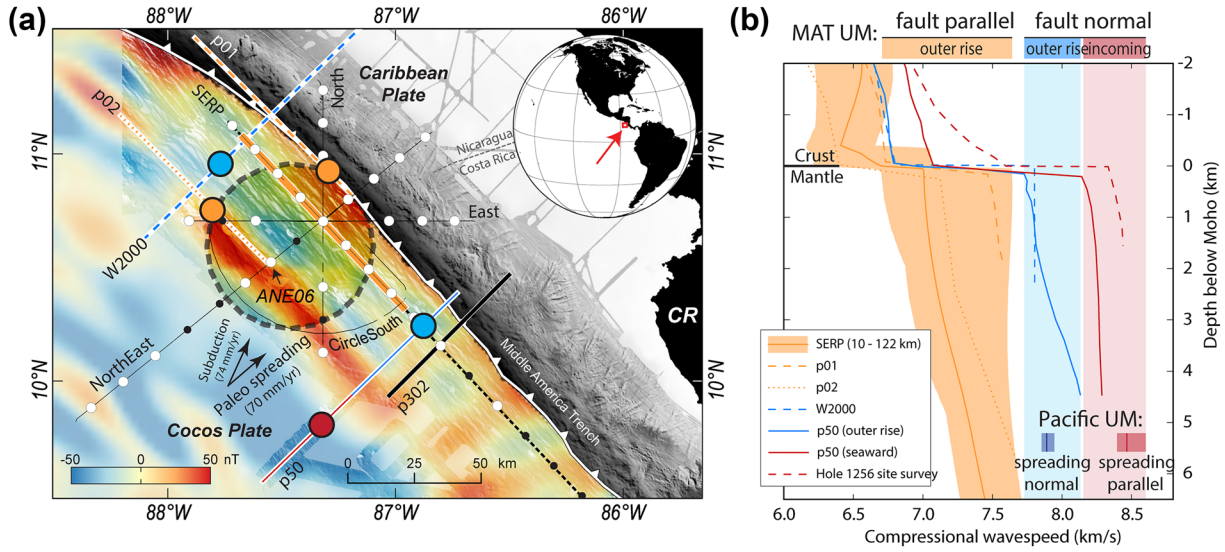

Figure 1. (a) Middle America Trench offshore Nicaragua and Costa Rica. Highlighted dashed circle is the bin used to select ray bottoming locations for the outer-rise anisotropy solutions. Thick lines mark published 2D seismic tomograms. Colored large circles mark the location of the profiles in (b). Small white and black circles mark OBS locations. White circles are sites used in the anisotropy solutions. OBS marked by black circles were omitted from analysis because of poor data quality or because they were outside the study area. Plate motion vectors are from Syracuse and Abers (2006). Basemap is shaded bathymetry (Weinrebe & Ranero, 2012) overlain with magnetic anomalies (Maus et al., 2009). CR—Costa Rica. (b) Velocity profiles from tomographic models along fault-normal (red and blue) and fault-parallel (orange) azimuths. Pacific wavespeed ranges are from upper-mantle anisotropy measurements. See Table 1 for velocity model references. UM—upper mantle.

$$V_{\mathrm{p}} = V_{\mathrm{p}}^{0} - 3.1\alpha_s \tag{1}$$

where V_{p}^{0} is a reference velocity for unaltered peridotite and α_s is the volume fraction of serpentine. Volume fraction serpentine can be converted to the weight fraction of mineralogically bound water w_h by (Carlson & Miller, 2003):

$$w_h = \frac{w_s \alpha_s \rho_s}{(1-\alpha_s)\rho_m + \alpha_s \rho_s} \tag{2}$$

where $w_s \approx 0.13$ is the weight fraction of water in 100% serpentine, $\alpha_s$is the volume fraction of serpentine, and $\rho_s \approx 2485$ kg/m^3 and $\rho_m \approx 3400$ kg/m^3 are the densities of serpentine and unaltered peridotite, respectively. For a constant $V_p^0 = 8.0$ km/s, for example, applying these relationships to the range of slow upper mantle velocities from outer rise tomography (Grevemeyer et al., 2018) implies that hydration ranges from ≤3.2% serpentine (≤0.31 wt% H_2O) at the Kuril Trench (Fujie et al., 2013) to as high as 26%–32% serpentine (~2.6–3.4 wt% H_2O) at the MAT offshore Nicaragua (Van Avendonk et al., 2011).

At the outer rise, upper-mantle seismic velocities may be slowed by widespread serpentinization, but relict, strain-induced anisotropy in the incoming plate and/or anisotropy created by the bending faults may also significantly affect mantle wave speeds (Figure 2). The choice of the reference velocity clearly affects the calculation of serpentinization and water content in Equations 1 and 2, and these sources of potential anisotropy should be accounted for in velocity-based hydration estimates.

In the Pacific upper mantle, azimuth-dependent delay times of upper-mantle refractions (Pn) indicate that compressional wavespeeds vary from ~7.9 km/s to as fast as ~8.6 km/s (Raitt et al., 1969; Kawasaki & Kon'no, 1984; Shearer & Orcutt, 1986). This ~7% anisotropy could result from a crystal-preferred orientation (CPO) in which ~22% alignment of individually anisotropic olivine grains creates a bulk anisotropy (Morris et al., 1969; Raitt et al., 1969; Shearer & Orcutt, 1986). CPO results from strain-induced grain rotation and recrystallization (Kaminski & Ribe, 2001, 2002) during flow at mid-ocean ridges (Marquart et al., 2007). Serpentine is also strongly anisotropic, and in the absence of continued strain, relict, spreading-induced

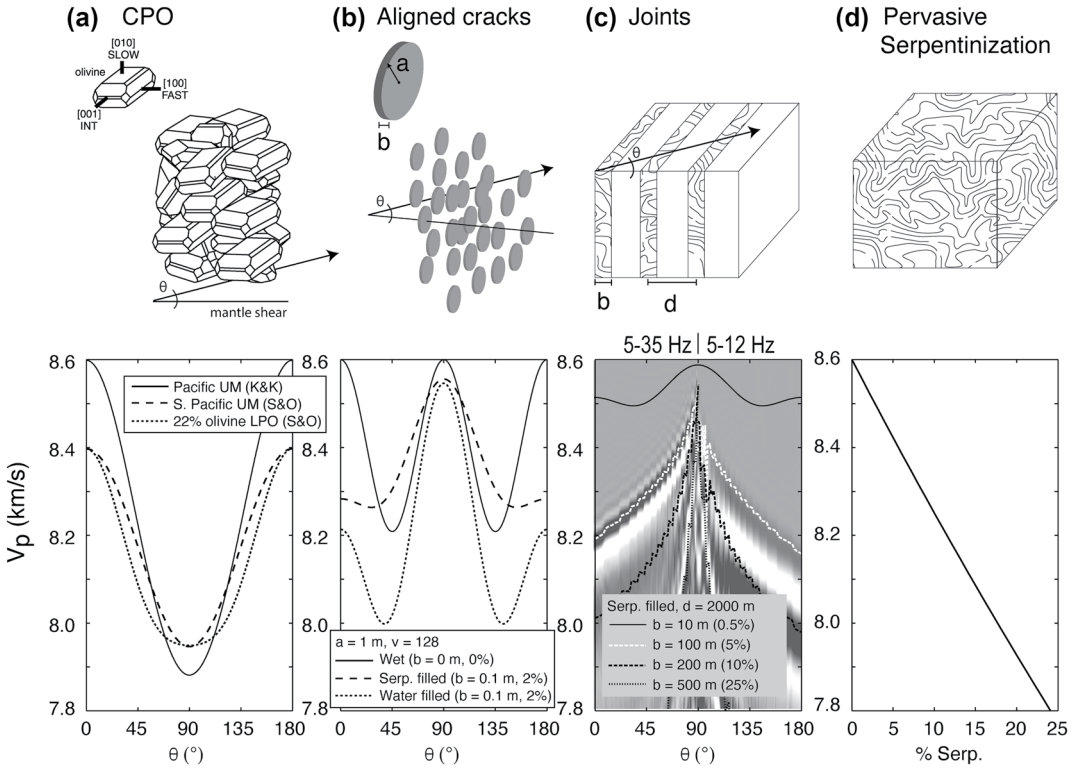

Figure 2. Comparison of apparent or quasicompressional wavespeeds (V_p) through an anisotropic versus pervasively serpentinized upper mantle (dunite). (a) Best-fit azimuthal wavespeed models for the uppermost mantle in the Pacific (Kawasaki & Kon'no, 1984), the south Pacific upper mantle (Shearer & Orcutt, 1986), and calculated velocities predicted for an olivine matrix with 22% crystal-preferred orientation (CPO) (Shearer & Orcutt, 1986). (b) Effective media theory (Hudson, 1981) calculations for qP in isotropic dunite (V_p = 8.6 km/s) with aligned, closed, but wet cracks and water- and serpentinite-filled cracks. (c) Geometrical effect of wide, serpentinite-filled, planar joints in isotropic dunite (V_p = 8.6 km/s) calculated by finite-frequency numerical simulation at 5–35 Hz (0°–90°) and 5–12 Hz (90°–180°) (Miller & Lizarralde, 2016). Background wavefield is for the 100-m-wide joint case. Also shown is the analytic solution of Hudson (1981) for 10-m-wide thin joints. (d) Effect of pervasive serpentinization (Christensen, 1966). Olivine crystal drawing in (a) is from Lev and Hager (2008).

anisotropic fabric may be progressively erased by widespread, uniform serpentinization at the outer rise (Horen et al., 1996; Wallis et al., 2011).

Like the Pacific Plate, the Cocos Plate subducting at the MAT offshore Nicaragua was produced at the East Pacific Rise, and the incoming slab is likely similarly anisotropic. At the MAT, magnetic anomalies indicate that the relict spreading direction is approximately perpendicular to both the trench and bending fault orientations. There, isotropic upper mantle velocities on two-dimensional tomograms are systematically slower in the trench-parallel direction than in the trench-perpendicular direction (Figure 1, Table 1), consistent with the expected orientation of relict anisotropy in the incoming plate. Setting V_p^0 = 7.9 km/s to account for anisotropy in the relict spreading-normal direction can reduce hydration estimates at the MAT to ~23% serpentinization (~2.3 wt% H_2O), but cannot explain all of the observed slowing.

A notable exception in the list of trenches with a slow upper mantle above is Cascadia. There, when spreading-induced anisotropy is measured in the incoming plate and accounted for, outer rise velocities indicate that the subducting upper mantle is nominally dry, perhaps because limited bend faulting limits the availability of water and/or because the young plate age and thick sediments cause the upper mantle to be hotter than at other subduction zones, preventing serpentinite stability (Canales et al., 2017).

Assuming that seawater can be delivered to upper mantle depths by outer-rise bend faulting (e.g., Faccenda et al., 2009), models based on fault dynamics and serpentinization kinetics suggest that hydration would re-

Table 1
Summary of Compressional Velocity and Wavespeed Anisotropy Models for Subducting Upper Mantle at the Middle America Trench

Model	Depth below Moho (km)	Wavespeed (km/s)		Reference
		Fault normal/spreading parallel (km/s)	Fault parallel/spreading normal (km/s)	
		Incoming upper mantle		
p50 (x = 30)	1.00–4.25	8.21–8.27	-	
Hole 1256 Site Survey	0.00–1.55	8.42–8.44	-	Shipboard Science Party (2003)
Pn Anisotropy (Pacific)	-	8.60	7.86	Kawasaki and Kon'no (1984)
Pn Anisotropy (South Pacific)	0.00–2.65	8.40	7.95	Shearer and Orcutt (1986)
22% CPO Anisotropy	-	8.40	7.86	Shearer and Orcutt (1986)
		Outer rise upper mantle		
SERP (x = 10–122 km)	1.00–5.00	-	6.75–7.64	Van Avendonk et al. (2011)
p01 (x = 70 km)	1.00–1.87	-	7.53–7.57	Ivandic et al. (2010)
p02 (x = 85 km)	1.00–5.00	-	7.16–7.57	Ivandic et al. (2010)
p50 (x = 115 km)	1.00–4.46	7.80–8.13	-	Ivandic et al. (2008)
W2000	1.00–2.35	7.80–7.81	-	Walther et al. (2000)
Pn Anisotropy	1.00–5.00	7.54–7.81	7.01–7.12	This study

Abbreviation: CPO, crystal-preferred orientation.

main localized within fault damage zones (e.g., Korenaga, 2017) and/or within alteration zones around faults (Hatakeyama et al., 2017). Free water and serpentinization within the crack-like porosity of damage zones is the simplest hydration distribution to justify. The ~1:1 scaling between displacement and damage zone width (e.g., Savage & Brodsky, 2011), implies that ~100–500 m fault offsets measured on and near the seafloor of the MAT outer rise (Ranero et al., 2003) should be surrounded by ~100- to 500-m-wide damage zones. These damage zones likely thin as fault offsets decrease and confining pressures increase with increasing depth, but, for upper mantle hydration to occur at the outer rise at all, bending faults must reach the mantle. The existence of faults in the outer rise upper mantle is supported by seismic reflection images of dipping reflectors in the mantle (Han et al., 2016; Ranero et al., 2003). We expect that, if free water can be pumped along these fault zones, it would react with fault-damaged mantle peridotite, filling crack-like porosity with serpentine (Korenaga, 2017).

Expanding serpentinization beyond fault zones requires a more complicated mechanism. For alteration to progress into unfractured mantle rock between faults, water supply must be sustained at the reaction front, even as the ~50% volume expansion of the reaction rapidly consumes porosity. At low enough confining pressures, volume expansion can continuously open new porosity, and, since serpentine is sufficiently permeable for seawater to diffuse at geologically rapid rates (~1 km/Myr at 300°C) through already-serpentinized mantle rock (Hatakeyama et al., 2017; Macdonald & Fyfe, 1985), the reaction may proceed to the ~80–100% alteration observed in seafloor and ophiolite peridotite exposures (Macdonald & Fyfe, 1985). In the outer rise hydration case, however, widespread serpentinization depends on a mechanism to drive horizontal flow of water from fault zones to the reaction front. This flow must overcome the strong positive pressure gradient between sublithostatic fault zone pressure, which is required for downward pumping to occur, and high confining pressure between the faults (Korenaga, 2017). Macdonald and Fyfe (1985) suggested that such "uphill" flow can be driven by low equilibrium vapor pressures (EVP) at the reaction front, which may be several orders of magnitude smaller than fault zone pressure (Ranero et al., 2003). In this mechanism, establishing a gradient between EVP and fault zone hydrostatic pressure requires the existence of water-filled porosity in both the serpentinized and unserpentinized mantle, a condition that is unlikely to be maintained as serpentinization rapidly consumes porosity (Korenaga, 2017). Even so, if EVP can sustain horizontal flow, how far serpentinization reaches between faults is controlled by the permeability of already serpentinized mantle and the duration of water access, a function of subduction rate. Recent laboratory measurements show that serpentine permeability is pressure dependent, causing the lateral extent of ser-

pentinization to decrease with depth (Hatakeyama et al., 2017). Although these permeability measurements are highly variable, intermediate values suggest that, for the ~0.5 Myr timescale during which the upper mantle is exposed to seawater by flow along bending faults at the MAT, serpentinized zones around faults may be ~400 m wide at the Moho and thin to ~100 m wide within ~5 km below the Moho (Hatakeyama et al., 2017), similar to the expected width of damage zones.

If upper mantle serpentinization is localized along planar fault zones (i.e., "joints"), wavespeeds are expected to be strongly anisotropic (Figure 2c), with slower wavespeeds in the fault-normal direction (Miller & Lizarralde, 2016). Even if widespread serpentinization extends uniformly between fault zones, wet fault zones and cracks oriented parallel to plate bending—which are required by the tectonic pumping model for seawater to reach the mantle in the first place—are also expected to produce a seismic anisotropy. In faulted rocks with aligned cracks or joints, anisotropy depends on the geometry and spacing of the cracks/joints and the stiffness of the unfaulted rocks and any void-filling materials (Anderson et al., 1974; Crampin, 1984; Gurevich, 2003; Hudson, 1981; Hudson et al, 1996, 2001; Thomsen, 1995). For example, effective media theory (Hudson, 1981) predicts that filling 2% crack-like porosity with serpentine in dunite ($V_p = 8.55$ km/s) causes compressional wavespeeds to vary from a minimum of 8.26 km/s in the crack-normal direction to 8.55 km/s in the crack-parallel direction, a 3.4% difference (Figure 2). Filling these same cracks with water produces 6.5% anisotropy, with an 8.00 km/s slow direction oriented at ~45° to crack faces. Even if the cracks are closed (i.e., 0% porosity), but wetted by water, dilation of the same crack distribution can produce a 4.7% anisotropy, also with slow directions at ~45° to the crack face.

Effective media theory for wavespeeds in cracked or jointed rocks (Hudson, 1981) assumes that the seismic wavelength is much larger than crack/joint width. This infinite-frequency approximation is appropriate for modeling media with thin cracks, but is not appropriate if, as predicted by models based on serpentine permeability (Hatakeyama et al., 2017), serpentinization is localized within ~100 to 400-m-wide joints: for the ~12 Hz frequency typical of Pn of arrivals in controlled-source studies (Van Avendonk et al., 2011), wavelength in an 8 km/s upper mantle is 667 m. Finite-frequency Fréchet sensitivity kernels for such a wave are ~10 km wide (Collins & Molnar, 2014).

Finite-frequency effects could have important implications for interpretations of wavespeeds in jointed media. In the infinite-frequency formulation (Hudson, 1981), wavespeeds in the joint (or crack) parallel direction approach the wavespeed of the media between the joints, implying that velocities measured along fault-parallel azimuths (e.g., Line SERP, Figure 1) are mostly insensitive to anisotropy from faults and can be used to constrain widespread alteration of the background mantle. Miller and Lizarralde (2016) modeled finite-frequency propagation through wide joints numerically, both for a uniform spacing of parallel joints and for the particular fault geometry observed at the MAT offshore Nicaragua, the study area of this paper. At 5–12 Hz and the ~2 km average spacing of bending faults at the MAT, apparent wavespeed is slowed by presence of at least 100-m-wide joints along all azimuths, in contrast with thin joints or cracks (Figure 2). As frequency approaches ~35 Hz, apparent wavespeed in the joint-parallel direction approaches the wavespeed of the background mantle, consistent with the thin crack/joint model. Bending faults are not perfectly planar, and wavefronts traveling tens of kilometers in the mantle must cross faults, adding to the fault-parallel slowing from finite-frequency sensitivity alone. When combined with a relict, spreading-induced anisotropy, the finite-frequency models suggest that wide joints may be responsible for all of the slowing observed in fault-normal and fault-parallel tomograms from the MAT (Miller & Lizarralde, 2016).

Controlled-source electromagnetic data collected at the MAT offshore Nicaragua suggest that bending-induced faulting produces an anisotropy in the electrical resistivity of the crust (Key et al., 2012). There, crustal resistivity decreases by up to a factor of five with the onset of outer-rise faulting. Resistivity in the incoming, unfaulted crust is isotropic, while the crust at the outer rise is strongly anisotropic with a conductive direction oriented parallel to the bending-induced faults. This observed decrease in resistivity and corresponding increase in anisotropy can be explained by an increase in porosity along parallel fault planes, supporting the hypothesis that these faults provide pathways for seawater to penetrate into the lithosphere. This electrical anisotropy and inferred fault-controlled-porosity structure corresponds to a seismic anisotropy in which wavespeeds are slower in the fault-normal direction than in the fault-parallel direction, opposite the orientation of anisotropy from a relict CPO in the incoming upper mantle. Thus, a transition between these two

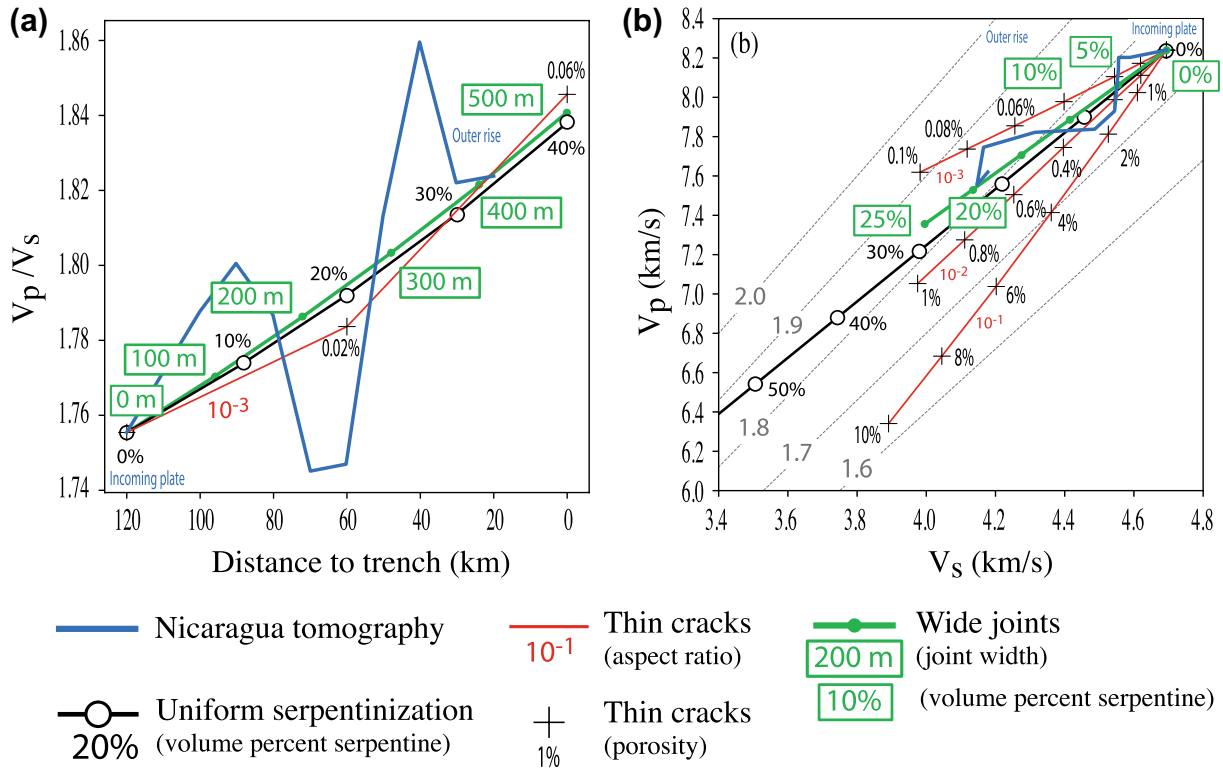

Figure 3. Similarity of V_p/V_s systematics in a pervasively serpentinized upper mantle to an upper mantle containing aligned cracks or wide joints. (a) Increase in upper mantle V_p/V_s ratio with distance to the trench observed in isotropic tomography from offshore Nicaragua (blue line) (Grevemeyer et al., 2018). Possible models that can explain this trend are an increase in uniform partial serpentinization (black line) (Carlson & Miller, 2003), an increase in thin crack-like porosity (Korenaga, 2017), or an increase in the width of large parallel joints (Miller & Lizarralde, 2016). (b) Same observations and models as in (a) plotted in V_p versus V_s space. Percent labels indicate porosity (cracks) or amount of serpentine by volume (uniform and joint models). Dashed lines are drawn along constant V_p/V_s ratios.

modes of anisotropy is expected to occur across the maximum depth extent of bending-induced faulting. Isolating these effects provides to a means for testing models of mantle hydration.

Along with slowing in V_p, a systematic decrease in shear velocity (V_s) and an increase in the ratio of V_p/V_s when approaching the trench along a single azimuth has been observed at the MAT offshore Nicaragua (Figure 3), as well as at other trenches globally (Fujie et al., 2018; Grevemeyer et al., 2018). V_s is sensitive to serpentinization in peridotites, and, for a uniformly altered mantle, an increase in V_p/V_s is consistent with an increase in volume percent of serpentine (Christensen, 2004), supporting the outer rise hydration hypothesis. Increasing porosity in a mantle with thin, small diameter (i.e., small aspect ratio), water-filled cracks can, however, also produce an increase in V_p/V_s, but with far less water than in the uniform hydration case (Korenaga, 2017). For example, the V_p/V_s increase observed offshore Nicaragua can be modeled by disc-shaped cracks with an aspect ratio of 10^{-3} and an increase in porosity from 0% in the incoming plate to only 0.06% (i.e., nominally dry) at the outer rise (Figure 3). Similarly, increasing the width of serpentine-filled joints from 0 to 400 m wide increases the proportion of serpentine sampled by a seismic wave and, in the fault-normal direction, can also reproduce the observed overall increase in the mean V_p/V_s of the bulk mantle (Figure 3). All three models—uniform serpentinization, wet cracks, and serpentine-filled joints—can fit V_p/V_s calculated from tomography equally well, and measurements of V_p/V_s along a single azimuth are not by themselves diagnostic of the particular distribution of hydration.

Cracks, joints, and a relict CPO may all be present in the upper mantle beneath the outer rise of subduction zones, and we expect that effective wavespeeds through such a composite material would include wavespeed variations from the different sources of anisotropy (Figure 2). Each of these potential sources of anisotropy

has a unique azimuthal dependence and measurements of effective wavespeeds should help constrain the distribution and extent of jointing, cracking, and/or widespread, pervasive hydration of the upper mantle.

3. Data and Methods

We measured upper mantle anisotropy under the outer rise of the MAT using a delay-time approach (Gaherty et al., 2004; Morris et al., 1969; Shearer & Orcutt, 1986). We first calculated the difference (i.e., residual or delay-time) between traveltimes through a reference isotropic velocity model and traveltimes picked on seismic data as a function of source-receiver azimuth. We then modeled the amplitude, orientation, and source of anisotropy (i.e., cracks/joints vs. CPO) by fitting delay times with models of wavespeeds in anisotropic media.

3.1. Effective Anisotropy Model

We assumed that the outer rise upper mantle can be modeled as a transversely isotropic media. Materials are considered transversely isotropic if they have an axis of symmetry that is normal to a plane of isotropy. This form is one of the simplest models of anisotropy, but it is applicable for modeling wavespeeds in mantle rocks at the outer rise. Olivine and pyroxene grains, the dominant minerals in the upper mantle, are individually transversely isotropic and are strongly anisotropic to the propagation of seismic waves. These minerals align along a CPO in the presence of strain (Jung & Karato, 2001; Karato, 2008; Zhang & Karato, 1995), and horizontal flow at seafloor-spreading centers causes the bulk upper mantle to be transversely isotropic with the fastest wavespeeds in the direction of spreading (Ismaïl & Mainprice, 1998; Kaminski & Ribe, 2001, 2002). As the plate cools and moves off axis, this CPO fabric is retained (Backus, 1965; Kawasaki & Kon'no, 1984; Shearer & Orcutt, 1986), and thus the upper mantle under the outer rise may also be transversely isotropic. At the outer rise, faults slip along reactivated abyssal-hill fabric or break along new, trench-parallel orientations if the abyssal-hill fabric is oriented at a sufficient angle (>25°) to the trench (Billen et al., 2007; Delescluse et al., 2008; Masson, 1991), producing sets of parallel fault planes. This symmetry causes wavespeeds in rocks with cracks or joints aligned along fault planes to also be transversely isotropic with slower wavespeeds in the fault-normal direction than in the fault-parallel direction (Anderson et al., 1974; Hudson, 1981). At the MAT, the relict plate spreading direction is also roughly normal to the trench and normal to strike of the bending-induced faults, and we assume the slow direction from faulting is generally aligned with the fast direction from a relict, spreading-induced CPO fabric. Characterizing the effective anisotropy from these competing effects was a principal goal of this study.

3.1.1. Wavespeeds in Transversely Isotropic Media

Expressions for seismic wavespeeds come from solutions to the equation of motion (Crampin, 1981; Thomsen, 1986), which, for small displacements from seismic waves traveling in anisotropic elastic media, is (Landau & Lifshiz, 2008):

$$\rho \frac{\partial^2 u_i}{\partial t^2} = \sum_{i,j,k} C_{ijkl} \frac{\partial^2 u_k}{\partial x_j \partial x_l} \tag{3}$$

where ρ is density, u_i is a displacement, t is time, x is the right-handed Cartesian coordinate, and C_{ijkl} is the elastic stiffness tensor. Defining a plane wave as:

$$u_i = a_i \exp\left[i\omega \left(t - \sum_k q_k x_k \right) \right] \tag{4}$$

where $\vec{a}$ is a vector defining the direction of the displacement and $\vec{q}$ is a slowness vector, and substituting Equation 4 into 3, yields (Karato, 2008):

$$\rho a_i = \sum_{j,k,l} C_{ijkl} q_j q_l a_k \tag{5}$$

Then, defining slowness as:

$$q_j = \frac{n_j}{V} \tag{6}$$

where V is the phase velocity of the seismic wave and $\vec{n}$ is a unit vector in the propagation direction, gives the Christoffel equation (Crampin, 1981; Karato, 2008):

$$\sum_k \left(T_{ik} - \rho V^2 \delta_{ik} \right) a_k = 0 \tag{7}$$

where

$$T_{ik} = \sum_{j,l} C_{ijkl} n_j n_l \tag{8}$$

For the case of transverse isotropy, we are interested in solving for phase velocity as a function of angle in the horizontal plane, defined here as $x_3 = 0$. If $x_3 = 0$ is a plane of symmetry, and θ is the angle between the x_1 direction and the displacement direction, Equation 7 can be solved for $V(\theta)$ by rotating the stiffness tensor C_{ijkl} into (Crampin, 1981; Karato, 2008):

$$C'_{ijkl} = \sum_{r,s,t,u=1}^{3} a_{ir} a_{js} a_{kt} a_{lu} C_{rstu} \tag{9}$$

where a_{ij} is the rotation matrix:

$$a_{ij} = \begin{bmatrix} \cos\theta & \sin\theta & 0 \\ -\sin\theta & \cos\theta & 0 \\ 0 & 0 & 1 \end{bmatrix} \tag{10}$$

This rotation is a multiplication of the fourth rank stiffness tensor with four matrices that each contain $\sin\theta$ and $\cos\theta$ terms, and thus exact solutions for $V(\theta)$ are a combination of sin and cos functions of up to 4θ (Karato, 2008).

The stiffness tensor is symmetric such that $C_{ijkl} = C_{jikl}$ and $C_{ijkl} = C_{ijlk}$, and the number of indices can be reduced from four to two using the Voigt notation where subscripts $11 \rightarrow 1$, $22 \rightarrow 2$, $33 \rightarrow 3$, $23 \rightarrow 4$, $32 \rightarrow 4$, $13 \rightarrow 5$, $31 \rightarrow 5$, $12 \rightarrow 6$, and $21 \rightarrow 6$. Then,

$$C_{ij} = \begin{bmatrix} C_{11} & C_{12} & C_{13} & C_{14} & C_{15} & C_{16} \\ C_{12} & C_{22} & C_{23} & C_{24} & C_{25} & C_{26} \\ C_{13} & C_{23} & C_{33} & C_{34} & C_{35} & C_{36} \\ C_{14} & C_{24} & C_{34} & C_{44} & C_{45} & C_{46} \\ C_{15} & C_{25} & C_{35} & C_{45} & C_{55} & C_{56} \\ C_{16} & C_{26} & C_{36} & C_{46} & C_{56} & C_{66} \end{bmatrix} \tag{11}$$

Phases in general anisotropic media propagate at an angle to the displacement front (i.e., wavefront). In weakly anisotropic media, however, such as a faulted upper mantle (Thomsen, 1986, 1987), the phase direction is approximately normal to the wavefront. Waves traveling in this quasinormal direction are referred to as quasiP waves (qP), and we define the phase velocity of this wave as $c = V_2 = V(n_2)$. In transversely isotropic media with $x_3 = 0$ as the plane of symmetry, $C_{15} = C_{56} = 0$, and the assumption of weak anisotropy implies that $C_{16} \ll C_{11}, C_{66}$ (Thomsen, 1986). Then, rotating $C_{ij} = C_{ijkl}$ about the x_3 axis, inserting the result into Equation 7, and solving for phase velocity yields (Crampin, 1981; Thomsen, 1986):

$$c^2 \approx A + B\cos 2\theta + C\sin 2\theta + D\cos 4\theta + E\sin 4\theta \tag{12}$$

Here, the coefficients depend on five independent elastic constants, defined by:

$$
\begin{aligned}
A &= \frac{3\left(C_{11}+C_{22}\right)+2\left(C_{12}+2C_{66}\right)}{8\rho} \\
B &= \frac{C_{11}-C_{22}}{2\rho} \\
C &= \frac{C_{16}+C_{26}}{\rho} \\
D &= \frac{C_{11}+C_{22}-2\left(C_{12}+2C_{66}\right)}{8\rho} \\
E &= \frac{C_{16}-C_{26}}{2\rho}
\end{aligned}
\tag{13}
$$

Increasing the level of symmetry reduces the azimuthal dependence in wavespeed. If $x_2 = 0$ is also a plane of symmetry, $C_{16} = -C_{26}$, wavespeed only varies with angle in the horizontal plane, and Equation 12 can be reduced to (Crampin, 1981):

$$
c^2 \approx A + B\cos 2\theta + D\cos 4\theta \tag{14}
$$

In isotropic media, for completeness, $C_{11} = C_{22}$, and Equation 14 becomes:

$$
c^2 \approx A = \frac{C_{11}}{\rho} = \frac{\lambda + 2\mu}{\rho} \tag{15}
$$

where $\lambda = -5C_{12}/3$ is the Lamé parameter and $\mu = C_{44} = \left(C_{11} - C_{12}\right)/2$ is the shear modulus.

3.1.2. Transverse Isotropy from Aligned Cracks

Hudson (1981) showed that isotropic solids containing a random distribution of aligned, disk-shaped cracks can be characterized as an effective transversely isotropic media. Wavespeeds are calculated by deriving effective elastic constants for waves propagating through a set of randomly distributed, yet aligned, cracks. For a material containing circular cracks with uniform radius a, thickness b, and ν cracks per unit volume, a crack number density can be defined as:

$$
e = \nu a^3 \tag{16}
$$

The equations below are first-order solutions that assume a small crack density (i.e., $e \ll 1$), and the crack thickness b is assumed to be much smaller than the seismic wavelength.

Cracks in the crust and upper mantle are likely to be filled with water and/or serpentine (Faccenda et al., 2009). For cracks filled with a weak material such as serpentine, wavespeed is given by (Hudson, 1981):

$$
c^2 \approx A_s + B_s\cos 2\theta + D_s\cos 4\theta \tag{17}
$$

where θ is the angle of propagation measured from the symmetry axis. The coefficients are:

$$
\begin{aligned}
A_s &= \alpha^2\left[1 - \frac{4e}{3}\left(\frac{\lambda^2 + 2\mu\lambda + (3/2)\mu^2}{\mu(\lambda+\mu)(1+K)} + \frac{2\mu}{(3\lambda+4\mu)(1+M)}\right)\right] \\
B_s &= -\frac{8}{3}\frac{e\alpha^2}{(1+K)} \\
D_s &= -\frac{e\alpha^2}{3}\left(\frac{2\mu}{(\lambda+\mu)(1+K)} - \frac{8\mu}{(3\lambda+4\mu)(1+M)}\right)
\end{aligned}
\tag{18}
$$

where $\alpha^2 = (\lambda + 2\mu) / \rho$ and λ, μ, and ρ are the Lamé parameter, shear modulus, and density of the uncracked solid, respectively. K and M are constants that describe the relative elastic stiffness of the rock matrix and the crack-filling material. These terms are given by:

$$K = \frac{1}{\pi}\frac{a\left(\kappa' + (4/3)\mu'\right)}{b\mu}\left(\frac{\lambda + 2\mu}{\lambda + \mu}\right)$$
$$M = \frac{4}{\pi}\left(\frac{a\mu'}{b\mu}\right)\left(\frac{\lambda + 2\mu}{3\lambda + 4\mu}\right) \tag{19}$$

where a is the radius and b is the width of the crack. μ' and $\kappa' = \lambda' + 2\mu' / 3$ are the shear and bulk moduli of the crack-filling material, respectively.

If the cracks are closed and dry (i.e., not wetted by a fluid), $\kappa' = \mu' = 0$ and $K = M = 0$. If the cracks are filled with a fluid, $\mu' = 0$, and

$$K_w = K(\mu' = 0) = \frac{1}{\pi}\frac{a\kappa'}{b\mu}\left(\frac{\lambda + 2\mu}{\lambda + \mu}\right)$$
$$M_w = M(\mu' = 0) = 0 \tag{20}$$

Then, the coefficients in Equation 17 become:

$$A_s(\mu' = 0) = \alpha^2\left[1 - \frac{4e}{3}\left(\frac{\lambda^2 + 2\mu\lambda + (3/2)\mu^2}{\mu(\lambda + \mu)(1 + K_w)} + \frac{2\mu}{(3\lambda + 4\mu)}\right)\right]$$
$$B_s(\mu' = 0) = -\frac{8}{3}\frac{e\alpha^2}{(1 + K_w)} \tag{21}$$
$$D_s(\mu' = 0) = -\frac{e\alpha^2}{3}\left(\frac{2\mu}{(\lambda + \mu)(1 + K_w)} - \frac{8\mu}{(3\lambda + 4\mu)}\right)$$

For serpentine or water-filled cracks in mantle peridotite, $O(B_s) = O(D_s)$, causing anisotropy to be periodic to 4θ. If the cracks are closed, but wetted by a fluid, wavespeed variations are only a function of 4θ, and Equation 17 becomes (Hudson, 1981):

$$c_w^2 \approx A_w + D_w \cos 4\theta \tag{22}$$

where

$$A_w = \alpha^2\left[1 - \frac{8}{3}e\left(\frac{\mu}{3\lambda + 4\mu}\right)\right]$$
$$D_w = \alpha^2\frac{8}{3}e\left(\frac{\mu}{3\lambda + 4\mu}\right) \tag{23}$$

3.1.3. Transverse Isotropy from Thin or Wide Joints

Zones of damage and/or alteration along planar faults zones can be characterized as cracks in which $a \gg b$ in the above equations. We refer to this geometry as "jointing." In materials with regularly spaced, parallel joints, the area of joint filling material per unit volume is $1/d$, where d is the spacing between the joints. This area is equivalent to $v\pi a^2$ for circular cracks, and Equation 17 is also valid for jointed materials, provided that the crack thickness b in Equation 19 is replaced with $4b/3$ (Hudson, 1981). In general, for crustal and mantle rocks, this factor of 4/3 causes $B_s > D_s$, and anisotropy from jointing is dominated by the 2θ term, in contrast to the stronger 4θ dependence in anisotropy from cracks.

The derivation of wavespeeds in cracked or jointed media summarized above assumes that the seismic wavelength is much larger than crack/joint width. At an upper mantle wavespeed of ~8 km/s and the ~12 Hz typical frequency of Pn arrivals in controlled-source studies (Van Avendonk et al., 2011), the seismic wavelength is >500 m. The infinite-frequency approximation is thus appropriate for modeling media with aligned cracks/joints with thicknesses on the order of meters, but is not appropriate for modeling the >100-m-wide damage/alteration zones that could exist along outer rise faults (e.g., Hatakeyama et al., 2017).

Miller and Lizarralde (2016) used numerical models to simulate finite-frequency wave propagation through 100, 200, and 500-m-wide joints. In these models, apparent wavespeed variation with azimuth through wide joints can also be approximated by a model of transverse isotropy (Equation 12), at least for the 5–35 Hz frequencies and 100–500 m joint widths that were modeled. For ~12 Hz Pn arrivals, apparent wavespeeds are slowed by the presence of at least 100-m-wide joints along all azimuths, in contrast with the prediction for thin cracks/joints that apparent wavespeed should approach the wavespeed in the background media in the crack/joint-parallel direction (Figure 2).

3.1.4. Effective Wavespeeds in Composite Fabrics

Wavespeeds in an outer rise upper mantle containing a combination of relict CPO fabric, cracks, and thin or wide joints can be modeled together as an effective transverse isotropic media. At the outer rise, conjugate sets of trenchward- and seaward-dipping faults create two sets of cracks and/or joints with symmetry axes aligned in the dip direction. Hudson (1981) showed that wavespeeds in materials with sets of cracks aligned in different orientations can be found by rotating C_{ijkl} for each set such that the x_3 axis is the axis of symmetry and summing the results to find the effective elastic stiffness tensor. If the different orientations are aligned at right angles to one another, wavespeeds are transversely isotropic with wavespeed given by Equation 12, but with effective stiffness constants substituted for C_{ij} in Equation 13. Aligned cracks are a particular case of transverse isotropy, and wavespeeds in rocks with an arbitrary combination of various sources (i.e., CPO, cracking, and jointing) of transverse isotropy oriented at right angles to one another would also yield effective wavespeeds in the form of Equation 12. At the outer rise offshore of Nicaragua, the relict spreading direction is approximately normal to the orientation of bending-induced faults (Figure 1), and we assume that the combination of a relict CPO fabric, aligned cracking, and/or parallel thin or wide jointing can be modeled as transversely isotropic.

3.2. Delaytime Inversion

We solved for models of transverse isotropy via least squares (LSQR) inversions of delay time of the upper mantle refraction phase Pn as a function of azimuth. For each unique raypath, we define delaytime as:

$$\tau_{k(ij)} = t_{k(ij)} - t^0_{k(ij)} - R_i - S_j - \epsilon_{k(ij)} \tag{24}$$

where the subscripts $i = [1,2,...,N]$ and $j = [1,2,...,M]$ refer to N and M unique receiver and source locations, the subscript $k(ij)$ refers to a unique path between the ith receiver and jth source, $t_{k(ij)}$ is the observed (picked) travel time, and $t^0_{k(ij)}$is the traveltime through a reference isotropic model (Figure 4). R_i and S_j are static corrections that account for errors in the isotropic model near individual receivers and sources. $\epsilon_{k(ij)}$ is the error from picking and remaining path-dependent misfit in the isotropic model. We set:

$$\tau_{k(ij)} = \frac{r_{k(ij)}}{\delta c\left(\theta_{k(ij)}\right)} \tag{25}$$

where r_{ij} is propagation distance in the horizontal symmetry plane. δc is wavespeed variation as a function of azimuth θ, which we set equal to $\delta_c = A_1 \cos 2\theta + A_2 \sin 2\theta + A_3 \cos 4\theta + A_4 \sin 4\theta$, where the coefficients are equivalent to the coefficients in Equation 12. Then, setting $\epsilon_{k(ij)} = 0$ in Equation 24 yields the objective function $T_{ij} = f_{ij}\left(\theta_{ij}, A_1, A_2, A_3, A_4, r_{ij}, R_i, S_j\right)$, or the inverse problem:

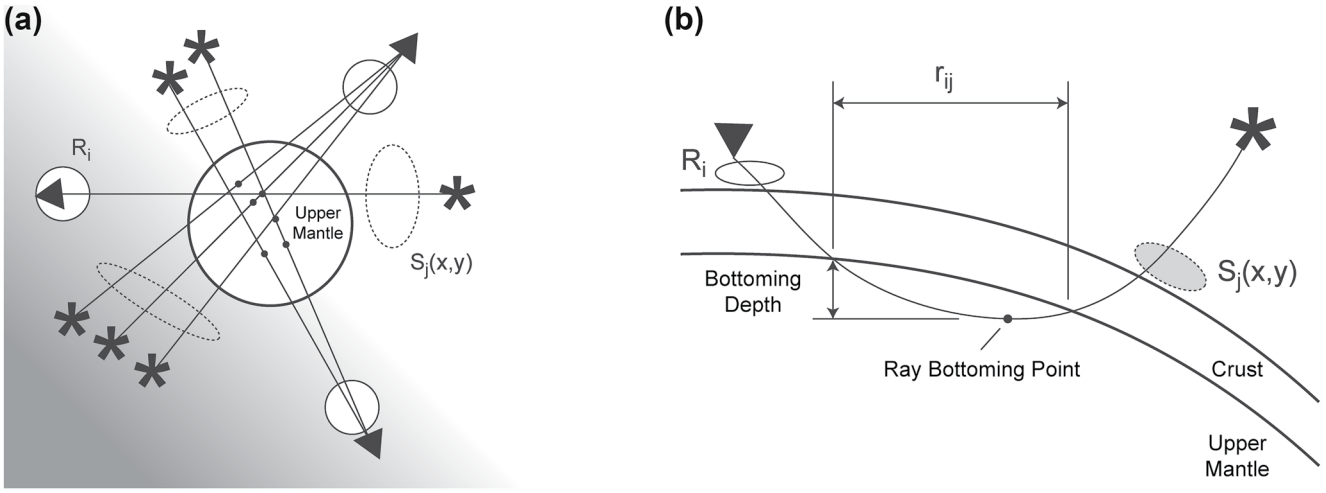

Figure 4. Schematic of model parameterization. (a) Map view. Receivers and sources are marked by triangles and stars, respectively. Circles represent receiver-side statics. The background gradient represents the source static polynomial surface S(x,y). The contribution of groups of sources to the source-static surface is indicated by the dashed ellipses. Ray bottoming points (i.e., the deepest point a ray reaches) are shown as black dots. (b) Profile view. r_{ij} is the horizontal distance traveled in the mantle between the ith receiver and jth source.

$$\mathbf{T} = \mathbf{G}\mathrm{m} \tag{26}$$

where **G** is a Jacobian matrix that relates model parameters in **m** to delay times in **T**. The quotient $r / \delta c$ in Equation 25 causes derivatives in the Jacobian to be functions of wavespeed coefficients, and a joint inversion for both wavespeeds and static corrections is thus nonlinear. The Jacobian becomes linear if the problem is formulated in terms of slowness $q = c^{-1}$. To order 4θ, slowness variations have the same form as wavespeed variations in Equation 12, and we set $\delta q = B_1 \cos 2\,\theta + B_2 \sin 2\,\theta + B_3 \cos 4\,\theta + B_4 \sin 4\,\theta$. The objective function is then:

$$f_{k(ij)} = r_{k(ij)} \delta q\left(\theta_{k(ij)}, B_1, B_2, B_3, B_4\right) - R_i - S_j \tag{27}$$

3.2.1. Seismic Data and Traveltime Picking

We used controlled-source ocean bottom seismograph (OBS) data collected during R/V *Marcus G. Langseth* and R/V *New Horizon* cruises MGL0807 and TC2NH as part of the 2008 TICO-CAVA2 experiment (Van Avendonk et al., 2011) (Figure 1). The OBS were all from the U.S. OBS Instrument Pool (OBSIP), and each carried a hydrophone and three-axis 4.5 Hz geophones. The *Langseth* source was a 108 L tuned air gun array fired every ~25–500 m along shot lines.

Crustal refraction (Pg), Moho reflection (PmP), and upper mantle refraction (Pn) picks were made on receiver gathers reduced at 8.55 km/s (Figure 5). For inline shots along Line NorthEast, a slab surface reflection (SxP) was also picked and used to constrain slab dip (Figure 6). All phases were used to develop the reference isotropic model, but only Pn picks were used in the anisotropy solutions. For picking, waveforms were minimally processed with a 75 ms gap deconvolution and a 3–15 Hz minimum-phase Butterworth filter. All shots located in the study region were used to initially cut and sort OBS data, but noise was reduced by culling shots with <30 s separation from the previous shot and stacking data from common-shot-point bins spaced every 500 m along shot lines. Azimuth and offset calculations used the mean source position for all traces in each common-shot bin. Data were visualized and picked by plotting receiver gathers along source lines in 3D (Figure 5e) using *OpendTect* (http://dgbes.com). 3D visualization of the wavefield on crossing lines aided in consistent phase identification, especially along shot lines with variable source-receiver azimuths. Phase consistency in picks was maintained by using *OpendTect's* seeded picking tool to

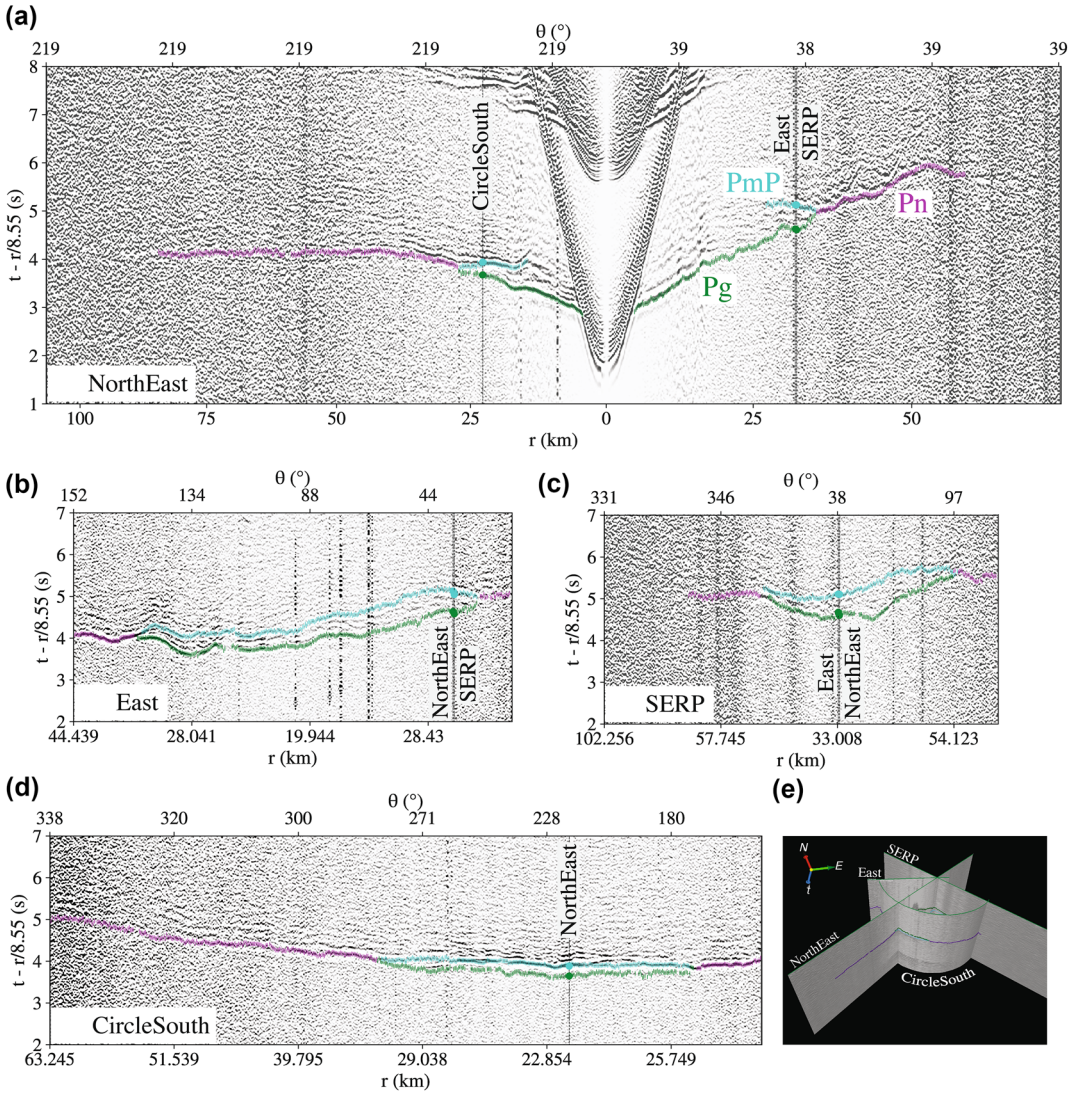

Figure 5. (a–d) Hydrophone data recorded at site ANE06 from shot Lines (a) NorthEast, (b) East, (c) SERP, and (d) CircleSouth. Traveltime picks are shown for Pg (green), PmP (blue), and Pn (purple). Pick ties are marked by colored dots at line crossings (vertical black lines). All data are plotted at the same horizontal scale with distance along the shot line. Source-receiver offset r and azimuth θ are labeled on the horizontal axes. Vertical axis is traveltime reduced by 8.55 km/s. (e) 3D view looking north at receiver gathers from (a–d) with traces plotted at source locations. See Figure 1 for line locations.

shift manual picks to the nearest peak positive amplitude within 30 ms of the manual pick. Both hydrophone and seismometer data were used to identify phases, but all picks were made on hydrophone data. Some OBS sites along line NorthEast and SERP (black circles in Figure 1) were omitted from analysis due to poor data quality, instrument failures, or because sites were outside the region of interest.

3.2.2. Isotropic Reference Model and Raytracing

We developed a 3D reference isotropic model that accounts for the general subduction zone structure. Crustal thickness, slab dip, forearc structure, and velocities were determined by forward modeling and 2D isotropic tomography along the trench-perpendicular Line NorthEast (Figure 6). The 2D model was then extended to three dimensions using bathymetry data (Weinrebe & Ranero, 2012) and by extruding the 2D velocity structure along the trench (Figure 7). Both 2D and 3D models used a 500 m horizontal and 100 m

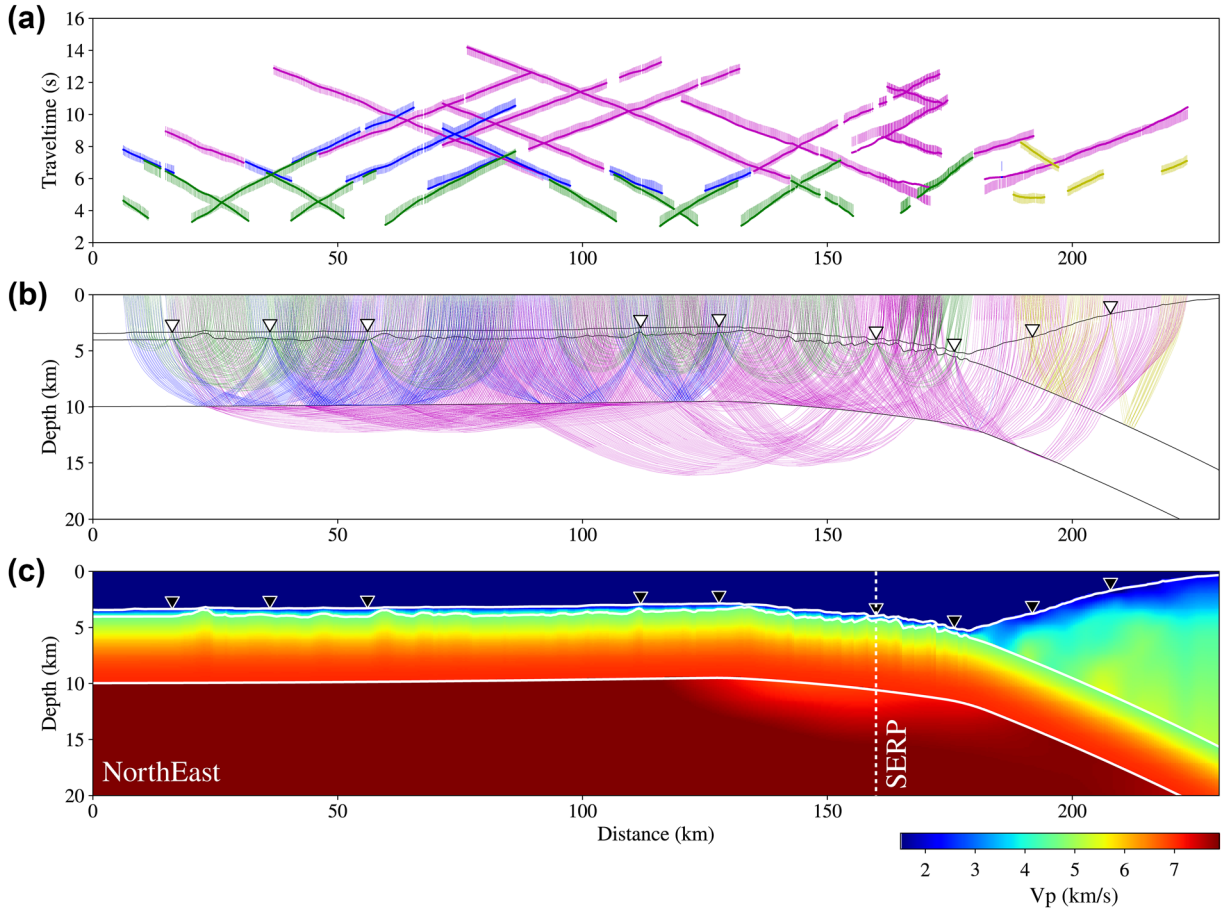

Figure 6. Two-dimensional isotropic velocity model and travel-times along Line NorthEast. (a) Dots mark predicted traveltimes calculated by raytracing. Picks are drawn with 300 ms error bars for visualization, but 50 ms errors were used for all phases in tomography. Predicted and picked times are colored as: upper mantle refraction Pn (magenta), Moho reflection PmP (cyan), crustal refraction Pg (black), and slab surface reflection SxP (yellow). (b) Raypaths through the model for the phases plotted in (a). Triangles mark ocean bottom seismograph locations. (c) 2D V_p model. The vertical line at the outer rise marks the crossing with Line SERP.

vertical grid spacing. To avoid introducing complexity from a poorly constrained 3D forearc structure, we replaced forearc velocities in the 2D model with a simple gradient in 3D. We note that the purpose of these models was to account for travel time variations due to overall structure, rather than provide detailed imaging of velocity. More detailed, local variations in structure are accounted for by source and receiver static terms in the inversion problem.

Tomography and raytracing were performed using a code developed by Van Avendonk et al., (2011) and A. Harding at Scripps Institute of Oceanography. Ray tracing for tomography and calculation of traveltimes through the reference isotropic model uses the shortest path method (Moser, 1991).

3.2.3. Azimuth Binning

Ray paths in this study are irregularly distributed as a function of azimuth, causing the inversion to preferentially fit data clumped along the "spoke" lines of the OBS array (Figure 8). We regularized the problem in azimuth by applying a smoothing operator Λ to Equation 26, giving:

$$\mathbf{T}\Lambda = \mathbf{G}\Lambda\mathbf{m} \tag{28}$$

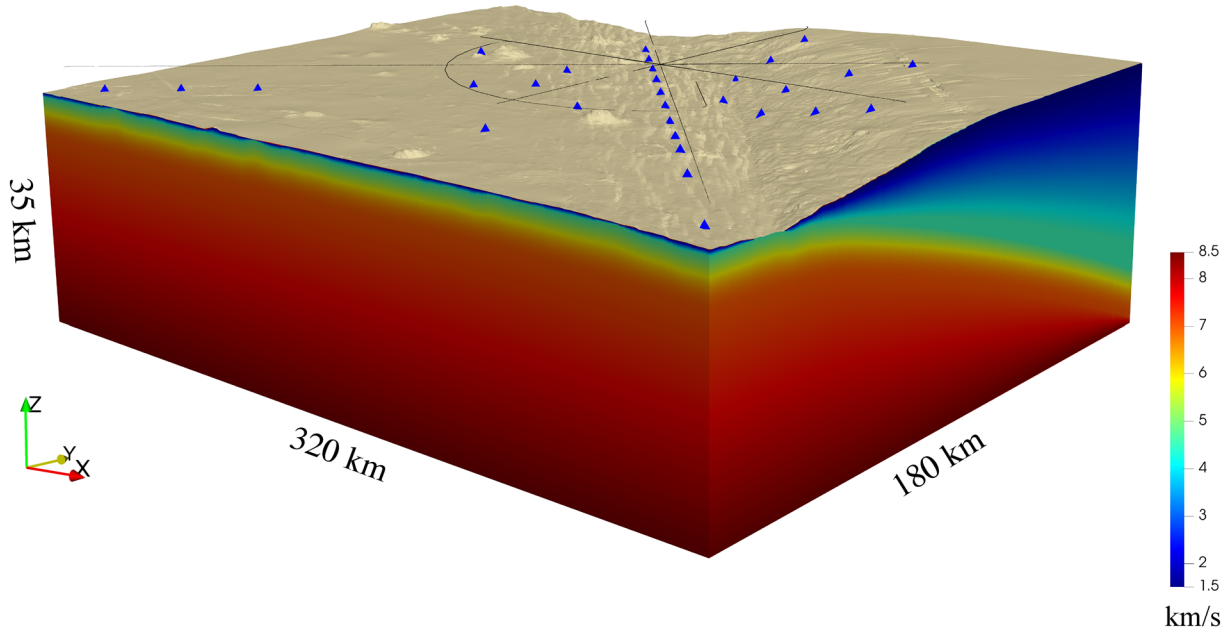

Figure 7. Perspective view looking northwest at the 3D reference isotropic model. Water layer is removed. OBS locations are marked by blue triangles. Shot locations are marked by black dots. Only sources and receivers used in the anisotropy solutions are shown.

Λ is a N-bin by K-raypath matrix that groups data into overlapping, triangular azimuth bins. For the nth bin and kth raypath, this operator is defined by

$$\Lambda_{nk} = \begin{cases} 1 - \dfrac{\left|\theta_k - n\Delta\theta\right|}{\Delta\theta \,/\, 2}, & \left|\theta_k - n\Delta\theta\right| \le \Delta\theta \,/\, 2 \\ 0 & \left|\theta_k - n\Delta\theta\right| > \Delta\theta \,/\, 2 \end{cases} \tag{29}$$

where $\Delta\theta$ is the bin width. Azimuth binning reduces the number of data rows in the inversion problem. In solutions with binning, we set $\Delta\theta \le 3°$, which keeps the total number of azimuth bins less than or equal to the number of model parameters in solutions with large numbers of static parameters. The anisotropy model in Equation 12 is periodic to at most 4θ and we thus mirrored delaytimes from $\theta > 180°$ such that $0° \le \theta \le 180°$ (Figure 8), which further limits the effect of experiment design on the anisotropy solution.

3.2.4. Source and Receiver Static Corrections

Each receiver recorded arrivals from hundreds of sources and a wide range of azimuths, enabling independent solutions for R_i in Equation 27. In contrast, each source was only recorded by ~1–10 receivers, and raypaths for common source groups only span a limited range of azimuths. Including independent source terms would allow the inversion to minimize misfit by varying source statics with azimuth, distorting anisotropy measurements. To limit the influence of any single source location on the solution, we regularized source statics by solving for a polynomial source-static surface:

$$S_j\left(x_j, y_j\right) = \sum_{q=0}^{p} \sum_{w=0}^{p-q} a_p x_j^q y_j^w \tag{30}$$

where x_j and y_j are easting and northing in Cartesian coordinates of the jth source. p is the degree of the polynomial, which we varied from 1 to 5. This parameterization adds $(1 + p)(2 + p)/2$model parameters to the inversion problem. Equation 30 forces the source static terms to vary slowly with position, accounting for regional changes in isotropic traveltimes (e.g., from changes in sediment thickness and/or velocity) that

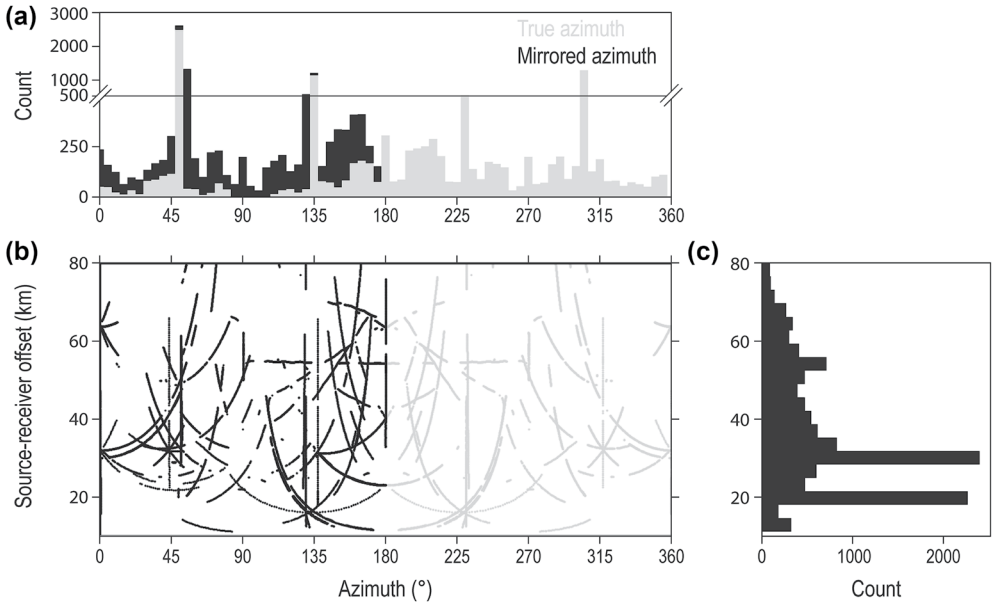

Figure 8. (a) Source-receiver azimuth and (c) offset distribution of all Pn picks used in anisotropy solutions. In (a) and (b), true source-receiver azimuths are plotted in gray, and mirrored azimuths (i.e., $\theta = 360 - \theta$ for $\theta > 180$) are plotted in black.

are not included in the reference model, while limiting azimuthal dependence. Mirroring azimuths also further minimizes the ability of source or receiver statics to bias the anisotropy solution.

3.2.5. Data Selection

To measure anisotropy at the outer rise, only Pn data with rays reaching a maximum depth (i.e., "bottoming points") within a 40-km-diameter circle centered on the outer rise were used in the inversions (Figure 1). Within this region, Pn rays with source-receiver offsets of 10–80 km sample the upper mantle from all azimuths (Figure 8).

4. Results

We inverted Pn delay times relative to a 3D isotropic model for upper mantle anisotropy at the outer rise of the MAT offshore Nicaragua. The results show the $\cos(2\theta)$ variations expected for azimuthal anisotropy (i.e., transverse isotropy), but the orientation of anisotropy rotates with depth (Figure 9). In the uppermost mantle (0–1 km beneath Moho), the fast direction is aligned NW/SE, parallel to plate-bending faults. At 1–5 km beneath the Moho, however, the fast direction is aligned approximately perpendicular to the faults, in the relict spreading direction, and the slow direction is fault parallel. Using absolute velocities from tomography along Line SERP (Van Avendonk et al., 2011), these anisotropy models indicate that, over 1–5 km below the Moho, wavespeeds are 7.67 km/s in the fast direction and 7.05 km/s in slow direction. These wavespeeds are ~7–8% slower over all azimuths, but the amplitude and orientation of anisotropy is similar to the models of unaltered Pacific upper mantle (Figure 9e). Below, we describe evidence for depth variation in anisotropy and sensitivity of the inversion results to model parameterization.

4.1. Variation of Upper Mantle Anisotropy with Depth

We tested for a depth dependence in anisotropy by separating data according to depth below Moho of ray bottoming points. Here, we define Moho depth as the crust-mantle boundary in the 3D reference model.

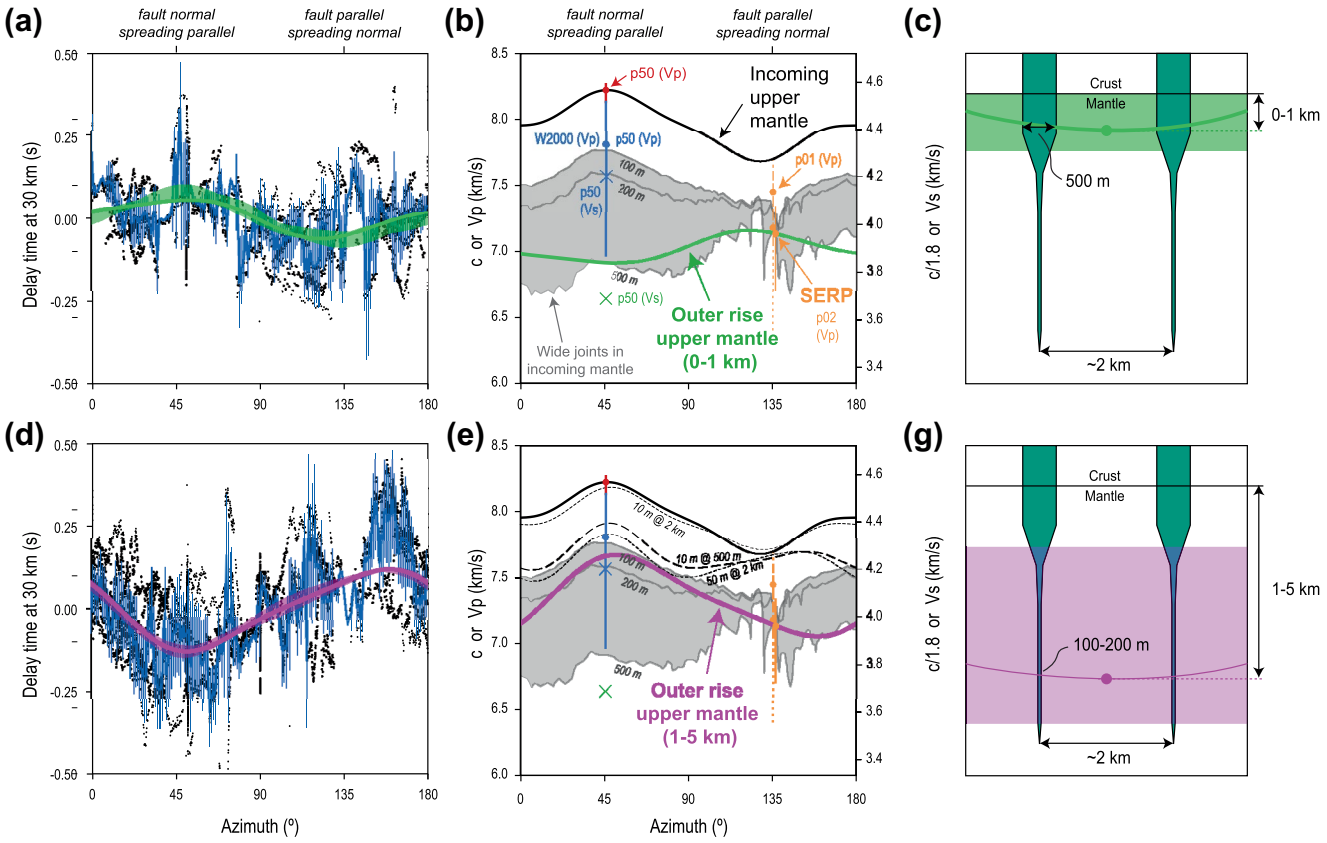

Figure 9. Measured anisotropy for Pn rays bottoming in the upper 0–1 km (a–c) and 1–5 (d–g) of the mantle at the MAT outer rise. (a, d) Best-fit azimuthal anisotropy models (green and magenta lines), delay times (black dots), and mean (blue line) and 1-standard deviation (blue error bars) for 1° azimuth bins. All delay times are corrected to 30 km of source-receiver offset using the best-fit anisotropy model. (b and e) Delay-time models from (a and d) converted to compressional wavespeed c for the upper 0–1 km (b, green) and 1–5 km (e, magenta) below Moho. Circles and vertical lines at ~45° and 135° mark the mean and range of V_p in upper 5 km of the mantle in the tomographic profile shown in Figure 6. "X" symbols are V_s measurements from just above (green) and below (blue) Moho at the outer rise on Line p50 (Grevemeyer et al., 2018). Thick black curve is a Pacific upper mantle anisotropy measurement (Shearer & Orcutt, 1986) shifted to align with p50 V_p seaward of the outer rise, which we assume represents the incoming Cocos-plate upper mantle. Gray lines and shaded region are wavespeeds from models of finite-frequency wave propagation through 100-, 200-, and 500-m-wide serpentine-filled joints arranged in the geometry of MAT bending faults and embedded in the Pacific mantle fabric (Miller & Lizarralde, 2016). Dashed black lines in (e) are predictions for 10- and 50-m-wide serpentine-filled planar joints at 500 m and 2 km spacings in the incoming upper mantle based on Hudson (1981). (c and g) Schematic showing the geometry of wide joints sampled by rays bottoming at 0–1 km (c) and 1–5 km (g) into the mantle.

In reality, the Moho is likely transitional, but the model-defined Moho is a useful datum that removes slab bending from absolute depth.

For a constant anisotropy, delay time along a single azimuth should scale linearly with propagation distance (Equation 25). For the MAT data, however, plotting delay-time versus source-receiver offset shows that Pn paths that bottom in the upper 1 km of the mantle, which includes source-receiver offsets less than ~37 km, show a distinctly different residual moveout velocity from rays that bottom at 1–5 km below Moho (Figure 10b). We thus divided results into these two depth ranges. Both depth ranges include rays from a wide range of azimuths, indicating that azimuthal coverage is not responsible for the change in slope of delaytime versus offset.

Inverting delaytimes from 0 to 1 km and 1–5 km below the Moho separately yields two distinctly different anisotropy solutions (Figure 10c). At 0–1 km below the Moho, anisotropy is weaker, with a fast direction aligned NW/SE. Between 1 and 5 km below the Moho, anisotropy is much more pronounced, and the fast direction rotates to NE/SW, ~90° from the uppermost mantle model.

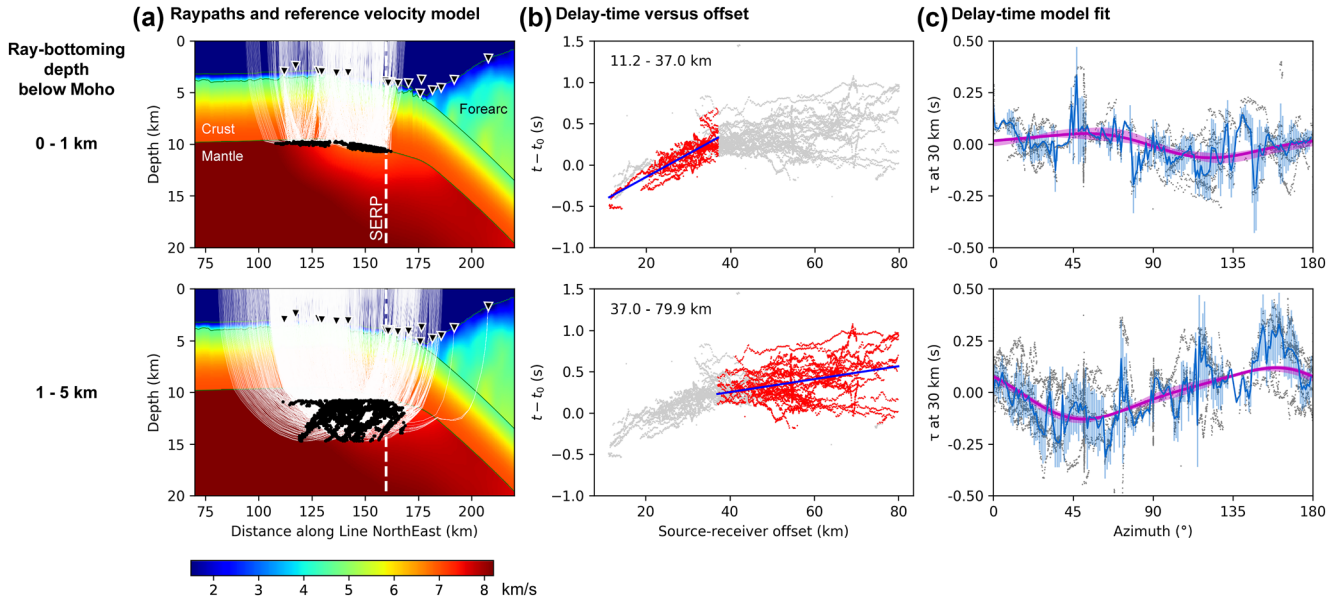

Figure 10. Anisotropy solution for the top 0–1 km of the oceanic upper mantle (top row) compared to the solution for the top 1–5 km (bottom row). (a) Pn raypaths (white lines) used in the depth-binned solution projected onto Line NorthEast. Note that the Moho dips slightly to the north and thus projected ray bottoming points appear closer than 1 km to the Moho on Line NorthEast. Background is an isotropic model along Line NorthEast. Triangles mark OBS locations. (b) Delaytime versus offset for all Pn data (gray dots) and data used for each depth bin solution (red dots). Blue line is a linear fit used to cull data that fall outside the 99.7% confidence interval. (c) Best-fit model of vertical-transverse isotropy (magenta curve) to delaytime data (gray dots). Blue error bars mark one standard deviation of data within 1º azimuth bins. The shaded magenta region marks the variation in 100 LSQR solutions calculated by jackknifing. LQSR, least squares.

4.2. Systematic Error from the Reference Model

We tested the effect of the 3D reference model on anisotropy solutions by also solving for anisotropy with simpler isotropic reference models. The simplest of these reference models is a linear moveout with source-receiver offset:

$$t^0_{k(ij)} = \frac{r_{k(ij)}}{c_0} \tag{31}$$

Here, c_0 is the moveout velocity, which we found by a LSQR fit to traveltime as a function of source-receiver offset. A slightly more complex isotropic reference model accounts for the effect of bathymetry on traveltime:

$$t^0_{k(ij)} = t^w_{k(ij)} + \frac{r_{k(ij)}}{c_0} \tag{32}$$

In this case, we calculated traveltime through the water column $t^w_{k(ij)}$ using seafloor piercing points of rays traced through the 3D model and a constant water velocity of 1,500 m/s.

The linear moveout model, with no bathymetric correction, is a poor fit to delay times (Figure 11). Including the bathymetric correction, which is well constrained by multibeam data, improves the fit, and, for the rays bottoming >1 km below the Moho, wavespeeds are faster in the fault-normal direction than in the fault-parallel direction. Using the full 3D reference model yields delay times with a similar root mean square amplitude, but reduces misfit in the anisotropy solution. The orientation of fast and slow directions is the same for delay times calculated with the bathymetric correction only and with the full 3D model, indicating that crustal and forearc structure in the reference model does not change the overall orientation of upper mantle anisotropy solutions.

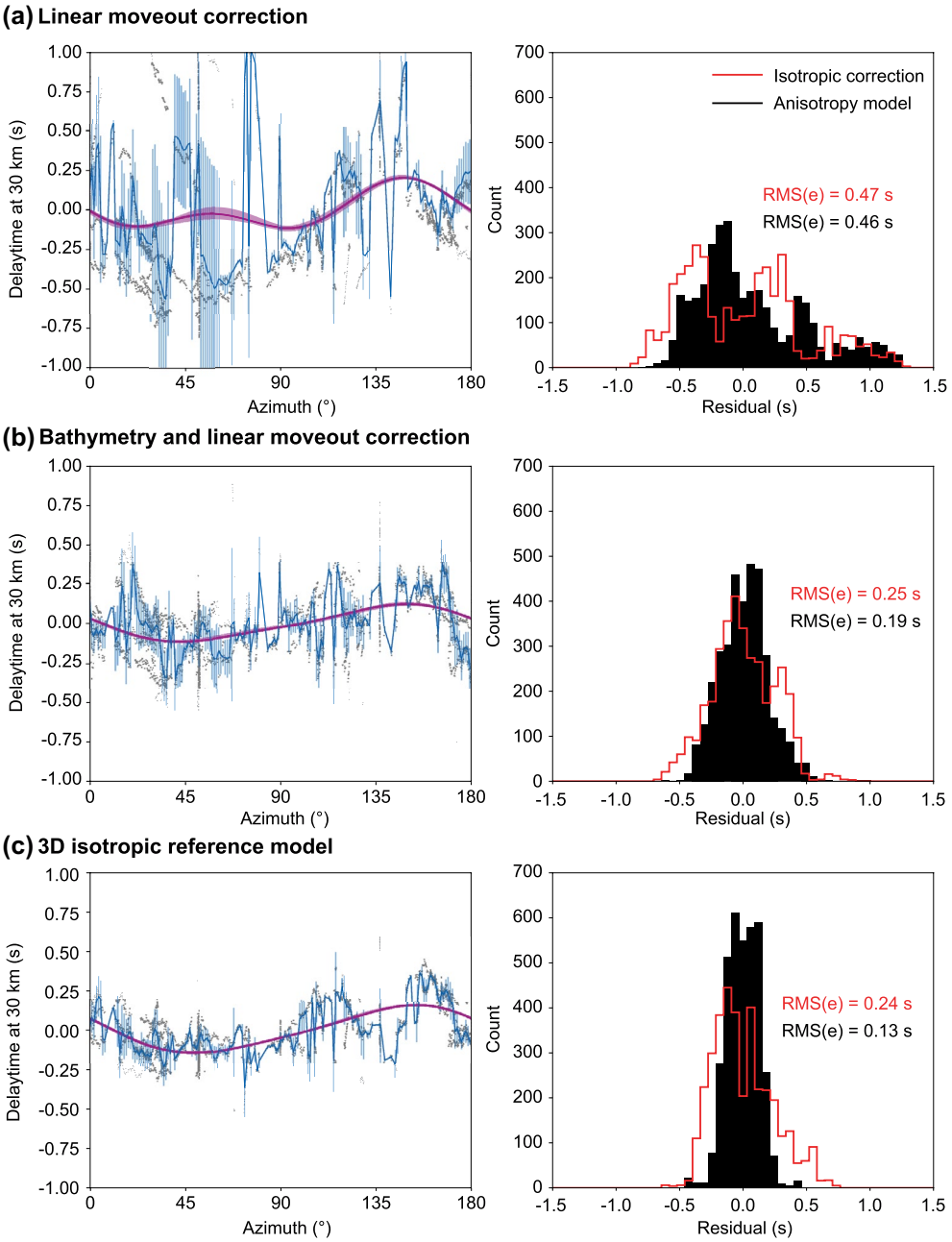

Figure 11. Comparison of anisotropy model solutions for 1–5 km below Moho with different isotropic reference models: (a) Linear moveout correction. (b) Bathymetry and linear moveout correction, and (c) 3D isotropic reference model. Left-hand column shows delaytimes at 30 km source-receiver offset for the anisotropy solution (magenta), Pn data binned by azimuth (blue line with one standard deviation error bars), and Pn data (gray dots). Right-hand column compares histograms of residuals for isotropic corrections (red) and anisotropy models (black).

4.2.1. Sensitivity to Model Regularization, Static Parameterization, and Choice of Preferred Models

We also tested the effect of different combinations of azimuth bin widths and static parameterizations on anisotropy solutions (Figures 12 and 13). For each parameterization, we estimated model uncertainty by jackknife resampling of the delay time data. Each jackknife set solved for 100 different models, with each

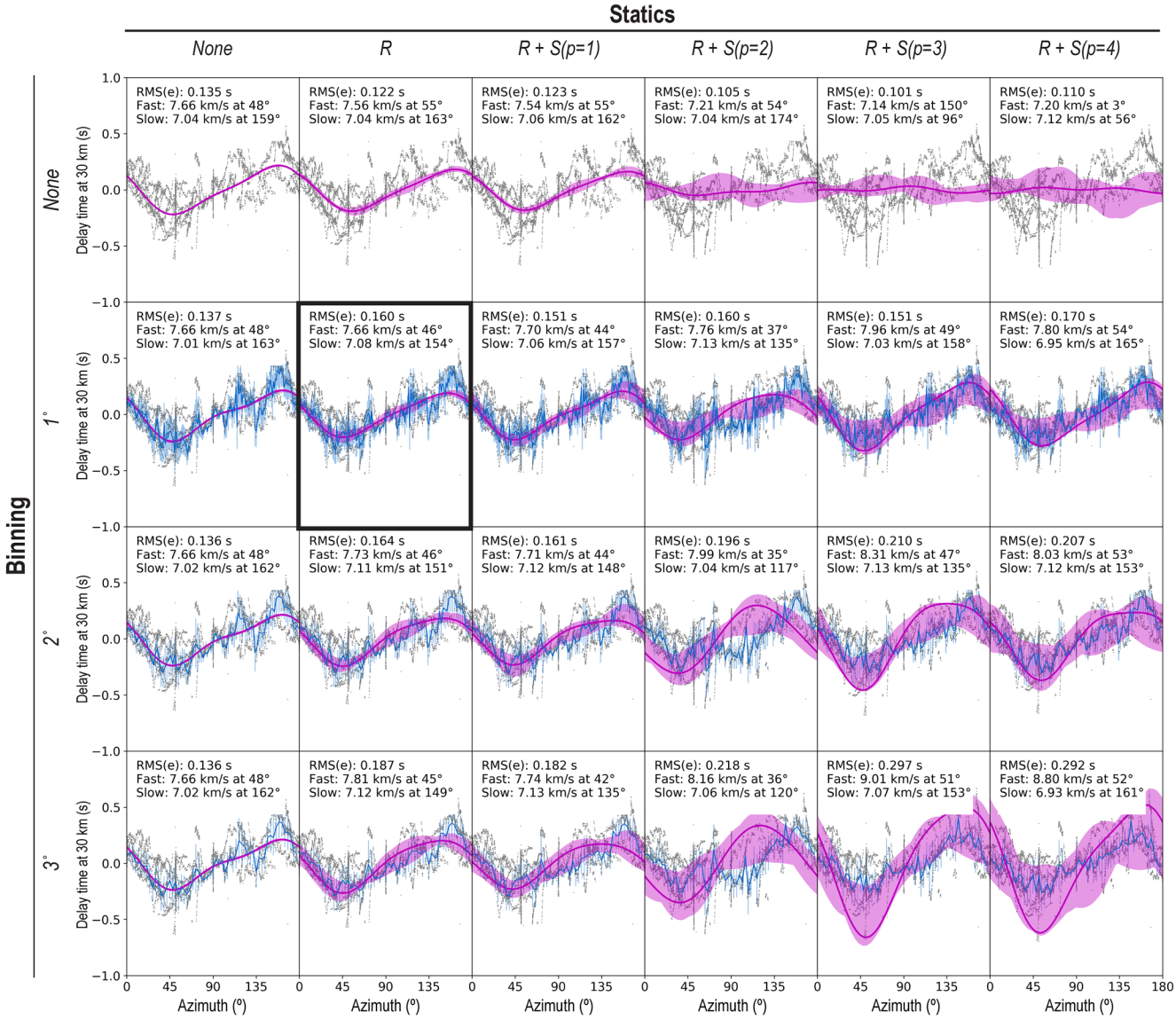

Figure 12. Effect of binning (rows) and static parameterization (columns) on delaytime solutions for Pn raypaths bottoming between 1 and 5 km of the Moho. Symbols are the same as in Figure 9d. All delay times are corrected to 30 km of source-receiver offset using the best-fit anisotropy model. Preferred model shown in Figure 9 is highlighted by the black box. See Figure 13 for corresponding static solutions. RMS(e) is the root-mean square of error.

using a random selection of 50% of the delaytime data. Variance in the jackknifing results is a measure of sensitivity to the input data and the effect of model regularization.

For the 1–5 km depth bin, almost all anisotropy models are dominated by a 2θ periodicity, with the fast axis oriented at 35–55° and generally aligned with the 45° orientation of the relict spreading direction. The exception to this trend is for models without binning and source static surface order $p \geq 2$. For $p \geq 2$, the source static surface is able to model 2θ periodicity, and the anisotropy seen in other parameterizations can be absorbed by the static terms. When azimuth binning is used, $p \geq 2$ source static surfaces amplify anisotropy. The variance in models found by jackknife resampling is also much larger in models with higher order static parameterizations, likely a consequence of the number of model parameters approaching the number of azimuth bins. Solutions are most stable with bin widths $\geq 1°$ and no static corrections, receiver statics alone, or with receiver statics and $p = 1$ source static surfaces. The solutions shown in Figure 9 were calculated with $1°$ bins and receiver statics only. These solutions are representative of the set of stable

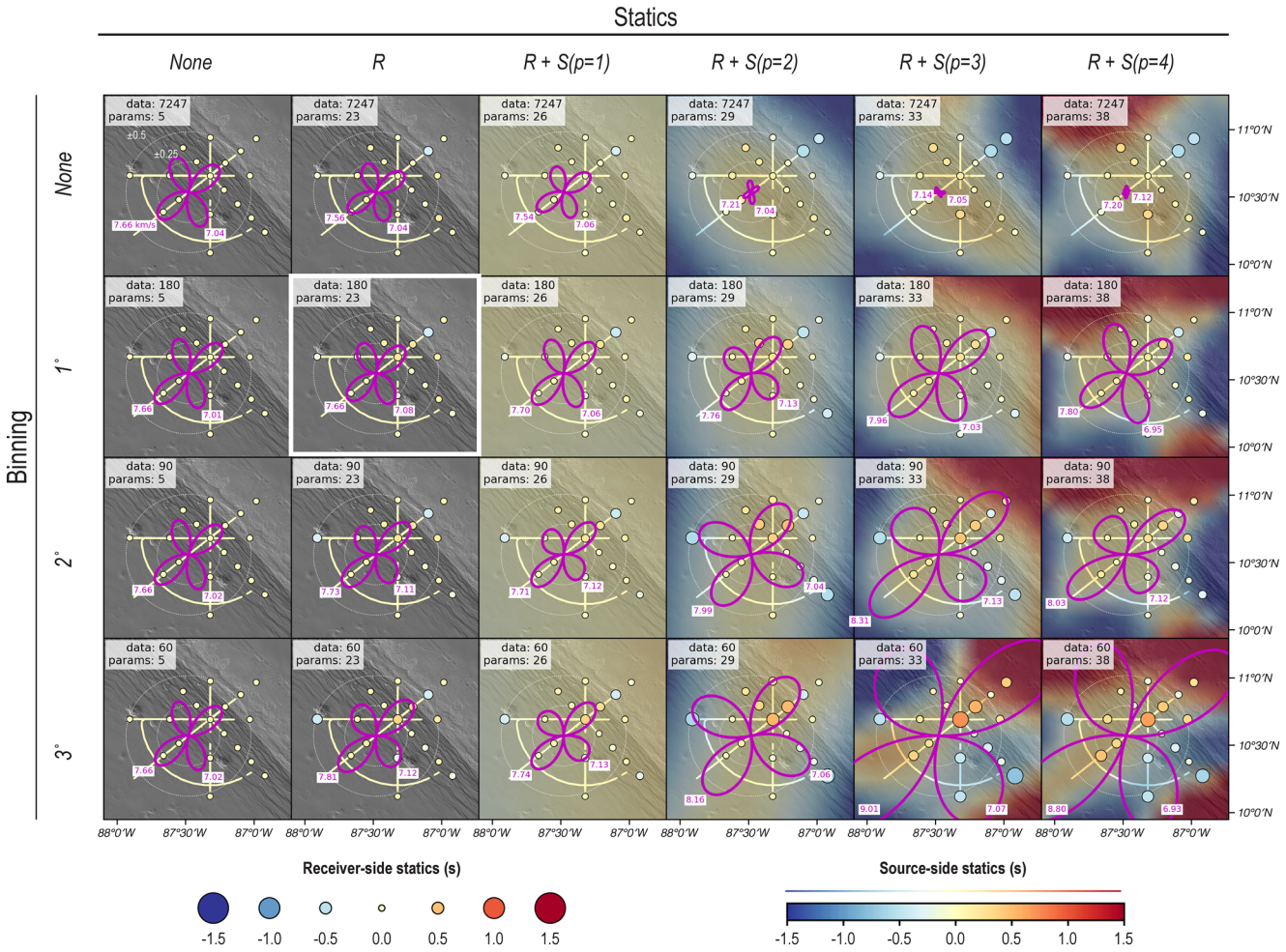

Figure 13. Effect of binning (rows) and static parameterization (columns) on static solutions and anisotropy models for Pn raypaths bottoming between 1 and 5 km of the Moho. Wavespeed variations $\delta c = c - c_0$ are plotted in polar coordinates centered on the outer-rise (magenta lines). Magenta text is the absolute wavespeed c in km/s of the fast and slow lobes. Receiver statics are marked by dots colored and scaled by the value of the static. Colored background is the source static surface and values applied to individual shots are marked by colored lines. Preferred model shown in Figure 9 is highlighted by the white box.

solutions, and we choose these solutions as preferred models. Slowness model coefficients for the models in Figure 9 are listed in Table 2.

5. Discussion

Anisotropy measurements from the MAT show that the outer rise upper mantle is azimuthally anisotropic and that this anisotropy changes with depth (Figure 9). Within 1 km of the Moho, the fast direction is aligned NW-SE, parallel to plate-bending faults. At 1–5 km beneath the Moho, however, a 7.67 km/s fast direction is aligned approximately perpendicular to the faults and a 7.05 km/s slow direction lies in the fault-parallel direction. This deeper pattern appears to preserve the relict anisotropy expected from the East Pacific Rise, but with absolute wavespeeds that are ~7%–8% slower over all azimuths. (Like the Pacific Plate, the Cocos Plate subducting offshore Nicaragua was produced at the East Pacific Rise, and we assume that the incoming, unaltered upper mantle is similarly anisotropic, with a fast direction aligned with the relict spreading direction [Shearer & Orcutt, 1986].)

The combination of overall slowing with preservation of inherited anisotropy orientation and amplitude is consistent with the Miller and Lizarralde (2016) finite frequency model of effective wavespeeds for 100- to 200-m-wide, parallel damage/alteration zones (i.e., joints) in a relict mantle fabric (Figure 9e). We suggest

Table 2
Anisotropy Parameters for Preferred Models in 9

	Anisotropy coefficient[b] (s/km)			
Depth below Moho[a]	B_1	B_2	B_3	B_4
0–1 km	4.1792E-04 ± 5.4873E-04	1.7657E-03 ± 4.2854E-04	1.1907E-04 ± 3.8040E-04	−4.3160E-04 ± 4.1506E-04
1–5 km	1.8166E-03 ± 1.8683E-03	−3.4367E-03 ± 1.8360E-03	7.2753E-04 ± 1.8547E-03	−2.5230E-04 ± 1.8069E-03

Note. Parameters shown here are for inversions with 1° bin widths, receiver-side statics, and no source-side statics.
[a]Range of depths below Moho of ray-bottoming points used in each inversion. [b]Coefficients in the slowness model $\delta q = B_1 \cos 2\theta + B_2 \sin 2\theta + B_3 \cos 4\theta + B_4 \sin 4\theta$. ± values are formal 95% confidence intervals.

that this model is the most likely explanation for anisotropy at 1–5 km below Moho. In contrast, wider zones of alteration or pervasive serpentinization would destroy or replace a relict mantle fabric (Wallis et al., 2011), yet the amplitude and phase of inherited anisotropy remains intact at the outer rise. Cracking can also produce anisotropy, but a uniform distribution of aligned wet or water-filled cracks create a 4θ periodicity (Figure 2), rather than the dominantly 2θ signal we observe, suggesting that cracking in the MAT upper mantle is localized within damage zones around bending faults (or relict damage zones, e.g., Korenaga, 2007) and only observed seismically as part of the extrinsic anisotropy of wide joints. Extrinsic anisotropy from wide joints also explains slow shear wave velocities (V_s) observed in the fault-normal direction at the MAT outer rise (Figure 3). Widening of joints can also produce the systematic increase in V_p/V_s observed at the outer rise (Grevemeyer et al., 2018) without invoking a change in crack aspect ratio, which is needed to produce the same trend with a uniform crack distribution (Korenaga, 2017).

Joints thinner than ~100 m can also produce an amplitude reduction and rotation of relict anisotropy, but constraining joint width depends on assumptions about joint spacing and the joint-filling material. If joints are filled with serpentine, as modeled by Miller and Lizarralde (2016), matching the anisotropy measurements with <100 m joints requires that joints are closer than the ~2 km fault spacing observed in bathymetry data from the MAT outer rise (Figure 9). Seismic images from the MAT outer rise (Ranero et al, 2003) and numerical models (Faccenda et al., 2009) suggest that the spacing of bending faults stays approximately constant with depth. MAT faults are thus likely be ~2 km apart at the Moho, meaning serpentine filled joints must be at least ~100 m wide. Nonetheless, anisotropy in materials with wide joints results from wavefronts crossing varying amounts of joint versus nonjoint material at different azimuths, and we expect that geometries equivalent to the ~5% volume fraction of a 100-m width and 2 km spacing would produce similar anisotropy patterns as predicted by the finite-frequency models, but with the same bulk serpentinite content. Analytic solutions for thin joints (i.e., long seismic wavelengths) (Hudson, 1981), which start to become appropriate for controlled-source studies at joint widths <100 m, show that the relict fast direction is preserved by 50-m-wide serpentine-filled joints spaced at 1 km, or 25-m-wide joints every 500 m (Figure 9). Similarly, filling joints with wet cracks allows for thinner joints and/or lower crack-like porosity. These analytic solutions assume perfectly planar joints, allowing wavefronts to avoid crossing joints and for apparent wavespeeds to approach the wavespeed of the background mantle in the fault-parallel direction, which is incompatible with observed slowing along Line SERP (Figure 9), regardless of joint spacing. In reality, wavefronts cross irregular fault geometries at the MAT, likely producing slowing along all azimuths and allowing for the possibility of thin, but closely spaced, joints.

At 0–1 km below Moho, wavespeeds are slowed by ~10–13% with respect to the incoming upper mantle and, as over 1–5 km, are also dominated by a cos(2θ) periodicity (Figure 9b). However, the 6.91 km/s slow and 7.16 km/s fast directions are aligned in the fault-parallel and fault-normal directions, opposite the alignment at 1–5 km below Moho. This rotation is consistent with the presence of 500-m-wide, serpentine-filled joints, which are wide enough to overprint relict mantle anisotropy in finite-frequency models (Miller & Lizarralde, 2016). Alternatively, more uniform serpentinization or widespread cracking may have destroyed relict anisotropy just below the Moho.

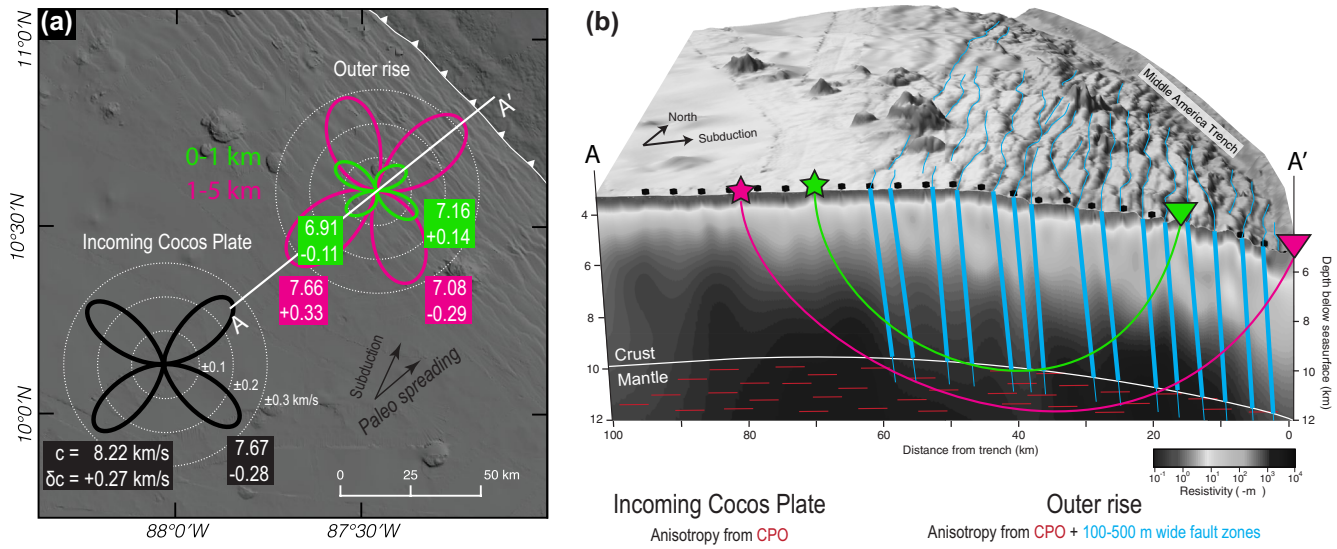

Figure 14. (a) Upper mantle wavespeed variation $\delta c = c - c_0$ plotted in polar coordinates for 0–1 km (green) and 1–5 km (magenta) below Moho at the outer rise compared with a model of δc for the incoming upper mantle (black) based on the Pacific upper mantle in (Shearer & Orcutt, 1986). Fast and slow lobes are labeled with absolute wavespeeds c and δc values. (b) Schematic showing the geometry of 500-m-wide (thick blue lines) 100-200 m-wide (thin blue lines) fault damage/alteration zones (i.e., joints) sampled by rays bottoming at 0–1 km (green) and 1–5 km (magenta) into the mantle. Background is resistivity modeled from controlled source electromagnetic data collected along Line NorthEast (Naif et al., 2015). Lighter shades correspond to regions of higher porosity, which are concentrated in the crust and along bending faults. Shaded bathymetry in (a) and (b) is based on (Weinrebe & Ranero, 2012).

Upper-mantle anisotropy at the MAT outer rise is best explained by the presence of wide joints aligned along bending faults, suggesting that hydrated damage/alteration zones are present in the upper 5 km of the mantle. However, the depth-dependence in anisotropy indicates joints thin rapidly from ~500 m wide in the upper 1 km of the mantle to ~100–200 m wide by 1–5 km below Moho (Figures 9c and 9g). This geometry is consistent with resistivity observations along Line NorthEast that show increased porosity along crustal faults, but a rapid decrease in porosity just below the Moho (Figure 14; Naif et al., 2015). Thinning of serpentinized fault zones within ~5 km of the Moho is also consistent with models in which hydration is limited to porosity within fault damage zones (Korenaga, 2017), which we expect to also thin as cumulative fault offset decreases and confining pressure increases with increasing depth in the mantle. Likewise, thinning from ~500-m- to ~100 to 200-m-wide at >1 km below Moho is consistent with the predicted width of alteration zones based on the depth dependence of serpentine permeability and timescales for water access at the outer rise (Hatakeyama et al., 2017).

Assuming fault zones are 100% serpentinized, extending the anisotropy-constrained 100- to 200-m-wide joint widths along faults observed on the seafloor at the MAT outer rise yields ~6.1–8.8% serpentine by volume, compared with estimates of up to ~20%–30% pervasive serpentinization based on isotropic tomography (Van Avendonk et al., 2011). This reduction is significant: a 6.1–8.8% serpentinized upper mantle contains just ~0.60 to 0.87 wt% H_2O (Miller & Lizarralde, 2016), compared with 3.5 wt% H_20 in a 30% serpentinized mantle (Carlson & Miller, 2003). The observed anisotropy could also be produced by filling the same joints with just 1% crack-like porosity, rather than 0% porosity serpentinite, but with even less water: water filled cracks within joints would contain only 0.02 to 0.03 bulk wt% H_2O (Miller & Lizarralde, 2016). Serpentinite samples from low-pressure settings commonly have high bulk porosities (Hatakeyama et al., 2017), suggesting that serpentinites in damage zones may also have high porosities and thus reduced velocities (Hatakeyama & Katayama, 2020). Increasing the porosity of serpentinites within joints yields bulk water estimates between the 0%-porosity-serpentinite- and wet-crack-filled joint models.

The joint model is based on observations from a single trench, but these constraints inform estimates of water input to subduction zones globally. In the ~24 Myr-old MAT slab, serpentine is stable to greater depths than in younger, hotter slabs (Ulmer & Trommsdorff, 1995), and seismic images (Ranero et al., 2003)—and

the anisotropy measurements—indicate that faults do penetrate into the upper mantle, providing a conduit for seawater infiltration. Yet, bulk upper mantle hydration is minimal and approaches nominally dry values observed in the hot, 5-9 Myr-old Cascadia slab mantle (Canales et al., 2017). This result implies that outer rise upper mantle hydration is primarily limited by the time available for water access (i.e., subduction rate) and parameters controlled by the dynamics of bend faulting (e.g., fault spacing, damage zone width, and pressure gradients) and kinetics of faulting and serpentinization (e.g., permeability and horizontal diffusion), rather than plate age (i.e., temperature). Slow isotropic velocities suggest that the MAT outer rise experiences the highest reported degree of alteration globally (Grevemeyer et al., 2018; Van Avendonk et al., 2011), but, since even these end-member velocities can be explained by a joint model and minimal hydration, the subducting slab upper mantle may be similarly dry globally. An exception may be at the oldest of slabs with steep subduction angles, such as at the Mariana Trench (Cai et al., 2018), where fault damage zones may be wider and bending faults and serpentine stability can extend deeper into the mantle, although subduction rate and fault spacing likely still act to limit hydration in these settings.

For the present configuration of subduction zones, assuming that the subducting upper mantle is nominally dry globally gives rates of water input to the deep mantle of ~1.5–4.5 × 10^8 Tg/Myr (Korenaga et al., 2017; Merdith et al., 2019; van Keken et al., 2011), ~60% less than if the upper mantle contained 2wt% H_2O (van Keken et al., 2011). In thermo-petrologic models, a MAT slab with a dry upper mantle, but a hydrated crust, contains ~33% less water overall and delivers ~33% less water to depths >100 km than one with even 2wt% upper mantle H_20 (van Keken et al., 2011), limiting how much water is delivered to the deep mantle, rather than cycled through the arc and forearc. As in these models, the MAT upper and lower crust is likely still hydrated by fluid flow along bending faults (Naif et al., 2015). However, upper crustal H_2O is largely expelled through the forearc, and, if the subducted upper mantle is dry, lower crustal gabbros would thus account for the majority of water delivery to depths >230 km (van Keken et al., 2011; Wada et al., 2012). A dry oceanic mantle and limited delivery of water to the deep mantle is consistent with geologic evidence for <360 m of sea level change over the Phanerozoic (Parai & Mukhopadhyay, 2012), although subduction flux also varies as tectonic plates reconfigure through time (Merdith et al., 2019), and secular variation in buoyancy and isostacy allows for substantial water influx to the mantle without causing long-term sea-level change (Korenaga et al., 2017).

The thermo-petrologic models assume that hydration is uniformly distributed within each layer, yet the mantle anisotropy results, as well as controlled source electromagnetic images of the crust (Naif et al., 2015), show that hydration is confined to fault zones. Models also suggest that localized hydration promotes shallow fluid release, releasing twice as much water at depths <100 km, where slab fluids are incorporated into the forearc and arc, than if the same bulk water content was distributed uniformly (Wada et al., 2012). Increased shallow release of mantle fluids along with the lack of a thermal control on mantle hydration may at least partly explain the narrow 2 to 6 wt% H_2O range observed in magma sources from arcs covering the global range of subducting plate ages (e.g., Mariana to MAT to Cascadia) (Plank et al., 2013).

6. Conclusions

Controlled-source measurements of seismic anisotropy constrain the lateral and vertical extent of upper mantle hydration by fluid flow along bending faults at the outer rise of the MAT. Within ~1 km of the Moho, anisotropy is measurably different from observations of unaltered uppermost mantle. At ~1–5 km below the Moho, however, the amplitude and orientation of relict upper mantle anisotropy is preserved. Since serpentinization alters anisotropy in mantle rocks, these observations indicate that serpentinization is minimal at depths >1 km below the Moho. Based on the anisotropy measurements and wave propagation models with a range of serpentinized fault zone widths, we propose that upper mantle hydration is limited to fault-parallel zones of alternation that are up to ~500 m wide near the Moho and thin rapidly to <100 m at depths greater than ~1 km below the Moho.

Confining hydration to fault zones reduces estimates of water storage in the subducting MAT upper mantle from ~3.5 wt% to <0.9 wt% H_2O. Since the intermediate thermal structure in the ~24 Myr-old MAT slab enables extensive serpentinization, the anisotropy measurements suggest that hydration is controlled by the dynamics of bend faulting and kinetics of serpentinization, rather than plate age/temperature. If upper

mantle hydration is limited globally, total water input to the deep mantle at subduction zones is expected to be ~2 × 108 Tg/Myr, which is at least ~60% less than the volume supplied by a pervasively hydrated upper mantle.

Data Availability Statement

The OBS data are publicly available under report number 08–012 at the IRIS Data Management Center (http://www.iris.edu). This work was supported by U.S. National Science Foundation grants OCE-0625178 and OCE-0841063. Any use of trade, firm or product name is for descriptive purposes only and does not imply endorsement by the U.S. Government.

Acknowledgments
We are grateful for the hard work and dedication of the technicians, crews, officers, and science party of R/V Langseth cruise MGL0807, who overcame many obstacles during Langseth's first science program, and also Trish Gregg and everyone aboard R/V New Horizon cruise TC2NH, which handled OBS operations. The OBS were provided and supported by the US Ocean Bottom Seismograph Instrument Pool (http://www.obsip.org) facilities at the Woods Hole Oceanographic Institution and the Scripps Institution of Oceanography. We thank D. Shillington, S. Naif, F. Klein, and U. ten Brink for many productive discussions and J. Kluesner, C. Ruppel, A. Trehu, and J. Korenaga for reviews of this manuscript.

References

Anderson, D. L., Minster, B., & Cole, D. (1974). The effect of oriented cracks on seismic velocities. *Journal of Geophysical Research*, *79*(26), 4011–4015. https://doi.org/10.1029/jb079i026p04011

Backus, G. E. (1965). Possible forms of seismic anisotropy of the uppermost mantle under oceans. *Journal of Geophysical Research*, *70*(14), 3429–3439. https://doi.org/10.1029/jz070i014p03429

Billen, M., Cowgill, E., & Buer, E. (2007). Determination of fault friction from reactivation of abyssal-hill faults in subduction zones. *Geology*, *35*(9), 819. https://doi.org/10.1130/g23847a.1

Cai, C., Wiens, D. A., Shen, W., & Eimer, M. (2018). Water input into the Mariana subduction zone estimated from ocean-bottom seismic data. *Nature*, *563*(7731), 389–392. https://doi.org/10.1038/s41586-018-0655-4

Canales, J. P., Carbotte, S. M., Nedimović, M. R., & Carton, H. (2017). Dry Juan de Fuca slab revealed by quantification of water entering Cascadia subduction zone. *Nature Geoscience*, *10*(11), 864–870. https://doi.org/10.1038/ngeo3050

Carlson, R. L., & Miller, D. J. (2003). Mantle wedge water contents estimated from seismic velocities in partially serpentinized peridotites. *Geophysical Research Letters*, *30*(5), 1250. https://doi.org/10.1029/2002gl016600

Christensen, N. I. (1966). Elasticity of ultrabasic rocks. *Journal of Geophysical Research*, *71*(24), 5921–5931. https://doi.org/10.1029/jz071i024p05921

Christensen, N. I. (2004). Serpentinites, peridotites, and seismology. *International Geology Review*, *46*(9), 795–816. https://doi.org/10.2747/0020-6814.46.9.795

Collins, J. A., & Molnar, P. (2014). Pn anisotropy beneath the South Island of New Zealand and implications for distributed deformation in continental lithosphere. *Journal of Geophysical Research: Solid Earth*, *119*(10), 7745–7767. https://doi.org/10.1002/2014jb011233

Contreras-Reyes, E., Becerra, J., Kopp, H., Reichert, C., & Díaz-Naveas, J. (2014). Seismic structure of the north-central Chilean convergent margin: Subduction erosion of a paleomagmatic arc. *Geophysical Research Letters*, *41*(5), 1523–1529. https://doi.org/10.1002/2013gl058729

Contreras-Reyes, E., Grevemeyer, I., Flueh, E. R., Scherwath, M., & Bialas, J. (2008). Effect of trench-outer rise bending-related faulting on seismic Poisson's ratio and mantle anisotropy: a case study offshore of Southern Central Chile. *Geophysical Journal International*, *173*(1), 142–156. https://doi.org/10.1111/j.1365-246x.2008.03716.x

Contreras-Reyes, E., Grevemeyer, I., Flueh, E. R., Scherwath, M., & Heesemann, M. (2007). Alteration of the subducting oceanic lithosphere at the southern central Chile trench-outer rise. *Geochemistry, Geophysics, Geosystems*, *8*(7), Q07003. https://doi.org/10.1029/2007gc001632

Contreras-Reyes, E., Grevemeyer, I., Watts, A. B., Flueh, E. R., Peirce, C., Moeller, S., &(2011). Deep seismic structure of the Tonga subduction zone: Implications for mantle hydration, tectonic erosion, and arc magmatism. *Journal of Geophysical Research*, *116*(B10), 341–18. https://doi.org/10.1029/2011jb008434

Contreras-Reyes, E., Ruiz, J. A., Becerra, J., Kopp, H., Reichert, C., Maksymowicz, A., &(2015). Structure and tectonics of the central Chilean margin (31°–33°S): implications for subduction erosion and shallow crustal seismicity. *Geophysical Journal International*, *203*(2), 776–791. https://doi.org/10.1093/gji/ggv309

Crampin, S. (1981). A review of wave motion in anisotropic and cracked elastic-media. *Wave Motion*, *3*(4), 343–391. https://doi.org/10.1016/0165-2125(81)90026-3

Crampin, S. (1984). Effective anisotropic elastic constants for wave propagation through cracked solids. *Geophysical Journal International*, *76*(1), 135–145. https://doi.org/10.1111/j.1365-246x.1984.tb05029.x

Delescluse, M., Montési, L. G. J., & Chamot-Rooke, N. (2008). Fault reactivation and selective abandonment in the oceanic lithosphere. *Geophysical Research Letters*, *35*(16), L16312. https://doi.org/10.1029/2008gl035066

Faccenda, M. (2014). Water in the slab: A trilogy. *Tectonophysics*, *614*(1–4), 1–30. https://doi.org/10.1016/j.tecto.2013.12.020

Faccenda, M., Gerya, T. V., & Burlini, L. (2009). Deep slab hydration induced by bending-related variations in tectonic pressure. *Nature Geoscience*, *2*(11), 790–793. https://doi.org/10.1038/ngeo656

Fujie, G., Kodaira, S., Kaiho, Y., Yamamoto, Y., Takahashi, T., Miura, S., &(2018). Controlling factor of incoming plate hydration at the north-western Pacific margin. *Nature Communications*, *9*(1), 3844. https://doi.org/10.1038/s41467-018-06320-z

Fujie, G., Kodaira, S., Yamashita, M., Sato, T., Takahashi, T., & Takahashi, N. (2013). Systematic changes in the incoming plate structure at the Kuril trench. *Geophysical Research Letters*, *40*(1), 88–93. https://doi.org/10.1029/2012gl054340

Gaherty, J. B., Lizarralde, D., Collins, J. A., Hirth, G., & Kim, S. (2004). Mantle deformation during slow seafloor spreading constrained by observations of seismic anisotropy in the western Atlantic. *Earth and Planetary Science Letters*, *228*(3–4), 255–265. https://doi.org/10.1016/j.epsl.2004.10.026

Grevemeyer, I., Ranero, C. R., Flueh, E. R., Kläschen, D., & Bialas, J. (2007). Passive and active seismological study of bending-related faulting and mantle serpentinization at the Middle America trench. *Earth and Planetary Science Letters*, *258*(3–4), 528–542. https://doi.org/10.1016/j.epsl.2007.04.013

Grevemeyer, I., Ranero, C. R., & Ivandic, M. (2018). Structure of oceanic crust and serpentinization at subduction trenches. *Geosphere*, *14*(2), 395–418. https://doi.org/10.1130/ges01537.1

Gurevich, B. (2003). Elastic properties of saturated porous rocks with aligned fractures. *Journal of Applied Geophysics*, *54*(3–4), 203–218. https://doi.org/10.1016/j.jappgeo.2002.11.002

Han, S., Carbotte, S. M., Canales, J. P., Nedimović, M. R., Carton, H., Gibson, J. C., &(2016). Seismic reflection imaging of the Juan de Fuca plate from ridge to trench: New constraints on the distribution of faulting and evolution of the crust prior to subduction. *Journal of Geophysical Research: Solid Earth*, *121*(3), 1849–1872. https://doi.org/10.1002/2015jb012416

Hatakeyama, K., & Katayama, I. (2020). Pore fluid effects on elastic wave velocities of serpentinite and implications for estimates of serpentinization in oceanic lithosphere. *Tectonophysics*, *775*, 228309. https://doi.org/10.1016/j.tecto.2019.228309

Hatakeyama, K., Katayama, I., Hirauchi, K., & Michibayashi, K. (2017). Mantle hydration along outer-rise faults inferred from serpentinite permeability. *Scientific Reports*, *7*(1), 13870. https://doi.org/10.1038/s41598-017-14309-9

Holbrook, W. S., Lizarralde, D., McGeary, S., Bangs, N., & Diebold, J. (1999). Structure and composition of the Aleutian island arc and implications for continental crustal growth. *Geology*, *27*(1), 31–34. https://doi.org/10.1130/0091-7613(1999)027<0031:sacota>2.3.co;2

Horen, H., Zamora, M., & Dubuisson, G. (1996). Seismic waves velocities and anisotropy in serpentinized peridotites from xigaze ophiolite: Abundance of serpentine in slow spreading ridge. *Geophysical Research Letters*, *23*(1), 9–12. https://doi.org/10.1029/95gl03594

Hudson, J. A. (1981). Wave speeds and attenuation of elastic waves in material containing cracks. *Geophysical Journal International*, *64*(1), 133–150. https://doi.org/10.1111/j.1365-246x.1981.tb02662.x

Hudson, J. A., Liu, E., & Crampin, S. (1996). The mechanical properties of materials with interconnected cracks and pores. *Geophysical Journal International*, *124*(1), 105–112. https://doi.org/10.1111/j.1365-246x.1996.tb06355.x

Hudson, J. A., Pointer, T., & Liu, E. (2001). Effective-medium theories for fluid-saturated materials with aligned cracks. *Geophysical Prospecting*, *49*(5), 509–522. https://doi.org/10.1046/j.1365-2478.2001.00272.x

Ismaïl, W. B., & Mainprice, D. (1998). An olivine fabric database: an overview of upper mantle fabrics and seismic anisotropy. *Tectonophysics*, *296*(1–2), 145–157. https://doi.org/10.1016/s0040-1951(98)00141-3

Ivandic, M., Grevemeyer, I., Berhorst, A., Flueh, E. R., & McIntosh, K. (2008). Impact of bending related faulting on the seismic properties of the incoming oceanic plate offshore of Nicaragua. *Journal of Geophysical Research*, *113*(B5), B05410. https://doi.org/10.1029/2007jb005291

Ivandic, M., Grevemeyer, I., Bialas, J., & Petersen, C. J. (2010). Serpentinization in the trench-outer rise region offshore of Nicaragua: constraints from seismic refraction and wide-angle data. *Geophysical Journal International*, *180*(3), 1253–1264. https://doi.org/10.1111/j.1365-246x.2009.04474.x

Jung, H., & Karato, S. (2001). Water-Induced Fabric Transitions in Olivine. *Science*, *293*(5534), 1460–1463. https://doi.org/10.1126/science.1062235

Kaminski, É., & Ribe, N. M. (2001). A kinematic model for recrystallization and texture development in olivine polycrystals. *Earth and Planetary Science Letters*, *189*(3–4), 253–267. https://doi.org/10.1016/s0012-821x(01)00356-9

Kaminski, É., & Ribe, N. M. (2002). Timescales for the evolution of seismic anisotropy in mantle flow. *Geochemistry, Geophysics, Geosystems*, *3*(8), 1–17. https://doi.org/10.1029/2001gc000222

Karato, S. (2008). *Deformation of earth materials. An introduction to the rheology of solid Earth*, Cambridge, UK: Cambridge University Press. https://doi.org/10.1017/CBO9780511804892

Kawasaki, I., & Kon'no, F. (1984). Azimuthal anisotropy of surface waves and the possible type of the seismic anisotropy due to preferred orientation of olivine in the uppermost mantle beneath the Pacific Ocean. *Journal of Physics of the Earth*, *32*(3), 229–244. https://doi.org/10.4294/jpe1952.32.229

Key, K., Constable, S., Matsuno, T., Evans, R. L., & Myer, D. (2012). Electromagnetic detection of plate hydration due to bending faults at the Middle America Trench. *Earth and Planetary Science Letters*, *30*, 35145–35253. https://doi.org/10.1016/j.epsl.2012.07.020

Korenaga, J. (2007). Thermal cracking and the deep hydration of oceanic lithosphere: A key to the generation of plate tectonics?. *Journal of Geophysical Research*, *112*(B5), B05408. https://doi.org/10.1029/2006jb004502

Korenaga, J. (2017). On the extent of mantle hydration caused by plate bending. *Earth and Planetary Science Letters*, *457*(C), 1–9. https://doi.org/10.1016/j.epsl.2016.10.011

Korenaga, J., Planavsky, N. J., & Evans, D. A. (2017). Global water cycle and the coevolution of the Earth's interior and surface environment. *Philosophical Transactions of the Royal Society A: Mathematical, Physical & Engineering Sciences*, *375*(2094), 20150393.

Landau, L. D., & Lifshiz, E. M. (2008). *Theory of elasticity*. Oxford, UK; New York, NY: Butterworth-Heinemann.

Lev, E., & Hager, B. H. (2008). Rayleigh-Taylor instabilities with anisotropic lithospheric viscosity. *Geophysical Journal International*, *173*(3), 806–814.

Macdonald, A. H., & Fyfe, W. S. (1985). Rate of serpentinization in seafloor environments. *Tectonophysics*, *116*(1–2), 123–135. https://doi.org/10.1016/0040-1951(85)90225-2

Marquart, G., Schmeling, H., & Čadek, O. (2007). Dynamic models for mantle flow and seismic anisotropy in the North Atlantic region and comparison with observations. *Geochemistry, Geophysics, Geosystems*, *8*(2), Q02008. https://doi.org/10.1029/2006gc001359

Masson, D. G. (1991). Fault patterns at outer trench walls. *Marine Geophysical Researches*, *13*(3), 209–225. https://doi.org/10.1007/bf00369150

Maus, S., Barckhausen, U., Berkenbosch, H., Bournas, N., Brozena, J., Childers, V., et al. (2009). EMAG2: A 2-arc min resolution Earth Magnetic Anomaly Grid compiled from satellite, airborne, and marine magnetic measurements. *Geochemistry, Geophysics, Geosystems*, *10*(8), Q08005. https://doi.org/10.1029/2009gc002471

Merdith, A. S., Atkins, S. E., & Tetley, M. G. (2019). Tectonic controls on carbon and serpentinite storage in subducted upper oceanic lithosphere for the past 320 Ma. *Frontiers of Earth Science*, *7*, 332. https://doi.org/10.3389/feart.2019.00332

Miller, N. C., & Lizarralde, D. (2016). Finite-frequency wave propagation through outer rise fault zones and seismic measurements of upper mantle hydration. *Geophysical Research Letters*, *43*(15), 7982–7990. https://doi.org/10.1002/2016gl070083

Morris, G. B., Raitt, R. W., & Shor, G. G. (1969). Velocity anisotropy and delay-time maps of the mantle near Hawaii. *Journal of Geophysical Research*, *74*(17), 4300–4316. https://doi.org/10.1029/jb074i017p04300

Moscoso, E., & Grevemeyer, I. (2015). Bending-related faulting of the incoming oceanic plate and its effect on lithospheric hydration and seismicity: A passive and active seismological study offshore Maule, Chile. *Journal of Geodynamics*, *90*, 58–70. https://doi.org/10.1016/j.jog.2015.06.00

Moser, T. J. (1991). Shortest path calculation of seismic rays. *Geophysics*, *56*(1), 59–67.

Naif, S., Key, K., Constable, S., & Evans, R. L. (2015). Water-rich bending faults at the Middle America Trench. *Geochemistry, Geophysics, Geosystems*, *16*(8), 2582–2597. https://doi.org/10.1002/2015gc005927

Parai, R., & Mukhopadhyay, S. (2012). How large is the subducted water flux? New constraints on mantle regassing rates. *Earth and Planetary Science Letters*, *317*(318), 396–406. https://doi.org/10.1016/j.epsl.2011.11.024

Peacock, S. A. (1990). Fluid processes in subduction zones. *Science*, *248*(4953), 329–337. https://doi.org/10.1126/science.248.4953.329

Planert, L., Kopp, H., Lueschen, E., Mueller, C., Flueh, E. R., Shulgin, A., et al. (2010). Lower plate structure and upper plate deformational segmentation at the Sunda-Banda arc transition, Indonesia. *Journal of Geophysical Research*, *115*(B8), 41–25. https://doi.org/10.1029/2009jb006713

Plank, T., Kelley, K. A., Zimmer, M. M., Hauri, E. H., & Wallace, P. J. (2013). Why do mafic arc magmas contain ~4wt% water on average? *Earth and Planetary Science Letters*, *364*, 168–179. https://doi.org/10.1016/j.epsl.2012.11.044

Raitt, R. W., Shor, G. G., Jr, Francis, T. J. G., & Morris, G. B. (1969). Anisotropy of the Pacific upper mantle. *Journal of Geophysical Research*, *74*(12), 3095–3109.

Ranero, C. R., Morgan, J. P., McIntosh, K., & Reichert, C. (2003). Bending-related faulting and mantle serpentinization at the Middle America trench. *Nature*, *425*(6956), 367–373. https://doi.org/10.1038/nature01961

Ranero, C. R., & Sallarès, V. (2004). Geophysical evidence for hydration of the crust and mantle of the Nazca plate during bending at the north Chile trench. *Geology*, *32*(7), 549–552. https://doi.org/10.1130/g20379.1

Rupke, L. (2004). Serpentine and the subduction zone water cycle. *Earth and Planetary Science Letters*, *223*(1–2), 17–34. https://doi.org/10.1016/j.epsl.2004.04.018

Savage, H. M., & Brodsky, E. E. (2011). Collateral damage: Evolution with displacement of fracture distribution and secondary fault strands in fault damage zones. *Journal of Geophysical Research*, *116*(B3), B03405. https://doi.org/10.1029/2010JB007665

Schmidt, M. W., & Poli, S. (1998). Experimentally based water budgets for dehydrating slabs and consequences for arc magma generation. *Earth and Planetary Science Letters*, *163*(1–4), 361–379.

Shearer, P. M., & Orcutt, J. A. (1986). Compressional and shear wave anisotropy in the oceanic lithosphere - the Ngendei seismic refraction experiment. *Geophysical Journal International*, *87*(3), 967–1003. https://doi.org/10.1111/j.1365-246x.1986.tb01979.x

Shillington, D. J., Bécel, A., Nedimović, M. R., Kuehn, H., Webb, S. C., Abers, G. A., et al. (2015). Link between plate fabric, hydration, and subduction zone seismicity in Alaska. *Nature Geoscience*, *8*(12), 961–964. https://doi.org/10.1038/ngeo2586

Shipboard Science Party. (2003). An in situ section of upper oceanic crust formed by superfast seafloor spreading at Site 1256. *Proceedings of the Ocean Drilling Program: Initial Reports* (Vol. 206, pp. 1–396). https://doi.org/10.2973/odp.pr.206.2003

Syracuse, E. M., & Abers, G. A. (2006). Global compilation of variations in slab depth beneath arc volcanoes and implications. *Geochemistry, Geophysics, Geosystems*, *7*(5), Q05017. https://doi.org/10.1029/2005gc001045

Thomsen, L. (1986). Weak elastic anisotropy. *Geophysics*, *51*(10), 1954–1966. https://doi.org/10.1190/1.1442051

Thomsen, L. (1987). Elastic anisotropy due to aligned cracks. *SEG Technical Program Expanded Abstracts 1987* (pp. 857–857). Society of Exploration Geophysicists.

Thomsen, L. (1995). Elastic anisotropy due to aligned cracks in porous rock. *Geophysical Prospecting*, *43*, 805–829.

Ulmer, P., & Trommsdorff, V. (1995). Serpentine Stability to Mantle Depths and Subduction-Related Magmatism. *Science*, *268*(5212), 858–861. https://doi.org/10.1126/science.268.5212.858

Van Avendonk, H. J. A., Holbrook, W. S., Lizarralde, D., & Denyer, P. (2011). Structure and serpentinization of the subducting Cocos plate offshore Nicaragua and Costa Rica. *Geochemistry, Geophysics, Geosystems*, *12*(6), Q06009. https://doi.org/10.1029/2011gc003592

van Keken, P. E., Hacker, B. R., Syracuse, E. M., & Abers, G. A. (2011). Subduction factory: 4. Depth-dependent flux of H2O from subducting slabs worldwide. *Journal of Geophysical Research*, *116*(B1), B01401. https://doi.org/10.1029/2010JB007922

Wada, I., Behn, M. D., & Shaw, A. M. (2012). Effects of heterogeneous hydration in the incoming plate, slab rehydration, and mantle wedge hydration on slab-derived H 2 O flux in subduction zones. *Earth and Planetary Science Letters*, *353–354*, 60–71. https://doi.org/10.1016/j.epsl.2012.07.025

Wallis, S. R., Kobayashi, H., Nishii, A., Mizukami, T., & Seto, Y. (2011). Obliteration of olivine crystallographic preferred orientation patterns in subduction-related antigorite-bearing mantle peridotite: an example from the Higashi–Akaishi body, SW Japan. *Geological Society, London, Special Publications*, *360*(1), 113–127. https://doi.org/10.1144/sp360.7

Walther, C. H. E., Flueh, E. R., Ranero, C. R., Huene, R. V., & Strauch, W. (2000). Crustal structure across the Pacific margin of Nicaragua:evidence for ophiolitic basement and a shallow mantle sliver. *Geophysical Journal International*, *141*(3), 759–777. https://doi.org/10.1046/j.1365-246x.2000.00134.x

Weinrebe, W., & Ranero, C. R. (2012). Multibeam bathymetry compilation of the Central America Pacific margin. *Integrated Earth Data Applications*. http://doi.org/10.1594/IEDA/100069

Zhang, S., & Karato, S. (1995). Lattice preferred orientation of olivine aggregates deformed in simple shear. *Nature*, *375*(6534), 774–777. https://doi.org/10.1038/375774a0